Composite Structures 298 (2022) 115990

Contents lists available at ScienceDirect

Composite Structures

journal homepage: www.elsevier.com/locate/compstruct

A three-dimensional theoretical model of free vibration for multifunctional sandwich plates with honeycomb-corrugated hybrid cores

Rui Kang [a,b], Cheng Shen [a,b,*], Tian Jian Lu [a,b,*]

[a] State Key Laboratory of Mechanics and Control of Mechanical Structures, Nanjing University of Aeronautics and Astronautics, Nanjing 210016, PR China
[b] MIIT Key Laboratory of Multifunctional Lightweight Materials and Structures (MLMS), Nanjing University of Aeronautics and Astronautics, Nanjing 210016, PR China

ARTICLE INFO

Keywords:
Honeycomb-corrugated hybrid core
Free vibration
Homogenization method
Three-dimensional elasticity theory

ABSTRACT

Combining honeycomb and corrugation to construct a multifunctional hybrid core for all-metallic sandwich construction can significantly enhance not only its stiffness and strength but also energy absorption and sound absorption relative to its honeycomb or corrugated sandwich counterpart of equal mass. However, how hybridization affects its vibration characteristics remains poorly understood, especially from a theoretical point of view. To address this deficiency, this study develops a theoretical model based on three-dimensional (3D) elasticity such that the free vibration of a hybrid-cored sandwich plate with arbitrary boundary conditions can be systematically evaluated. Based on micromechanics analysis of the representative volume element, the effect of honeycomb-corrugated coupling is duly accounted and the incorrectly expressed equivalent constitutive of hexagonal honeycombs in previous studies are modified. The model is validated against 3D finite element simulations. The natural frequencies of a honeycomb-corrugated sandwich construction are consistently higher than its honeycomb or corrugated sandwich counterparts, due mainly to mechanisms: honeycomb filling suppresses local vibration of face sheets and corrugated members, and mutual constraint of honeycomb and corrugation enhance the flexural rigidity of hybrid core. The proposed theoretical model can be easily extended to analyze other cases, such as sound radiation and sound insulation of hybrid sandwiches.

1. Introduction

All-metallic corrugated sandwich constructions are widely used in transportation, construction, and aerospace engineering fields due to their ultralightweight, good structural performance (stiffness/strength and energy absorption), active cooling capability, sound absorption (one face sheet as well as corrugated members perforated with periodically distributed micro-holes), ease of fabrication and reparability, relatively low manufacturing costs [1–8]. However, in the absence of lateral support, the relatively thin corrugated members and face sheets are prone to local buckling under quasi-static or dynamic loading, thus limiting the load-bearing and energy absorbing capacity of corrugated sandwich structures.

To address the issue, filling the interstices of the corrugated core with other materials has been envisioned as a potential approach to enhance the mechanical performance of the sandwich. For example, Vaziri et al. [9] proposed to fill all-metallic corrugated sandwich plates with cellular polymer foams. However, a rather disappointing conclusion was obtained, as their study demonstrated that a foam-filled sandwich plate, when subjected to impulsive loading, exhibits no obvious load-bearing advantage compared with its unfilled counterpart of equal mass. This may be because the polymer foam selected as filler is mechanically rather weak and hence cannot provide sufficient lateral support for metallic corrugated members against plastic yielding and buckling. Subsequently, to improve the structural performance, all-metallic corrugated sandwich structures filled with cellular metallic foam were extensively studied [10–16]. Compared with empty corrugated sandwiches, the rigidity, strength, and energy absorption of metal foam-filled corrugated structures are indeed significantly improved, for the strong lateral support of metallic foam-filling to metallic corrugated members delays their plastic yielding and local buckling. Nonetheless, another drawback of the foam-filling approach emerges: the mass of hybrid foam-corrugated core is also significantly increased by the filled metallic foams, which makes the structural advantage of a metal foam-filled corrugated sandwich not obvious compared to its empty counterpart of equal mass.

* Corresponding authors at: State Key Laboratory of Mechanics and Control of Mechanical Structures, Nanjing University of Aeronautics and Astronautics, Nanjing 210016, PR China.
E-mail addresses: cshen@nuaa.edu.cn (C. Shen), tjlu@nuaa.edu.cn (T.J. Lu).

https://doi.org/10.1016/j.compstruct.2022.115990
Received 23 February 2022; Received in revised form 9 June 2022; Accepted 22 July 2022
Available online 26 July 2022

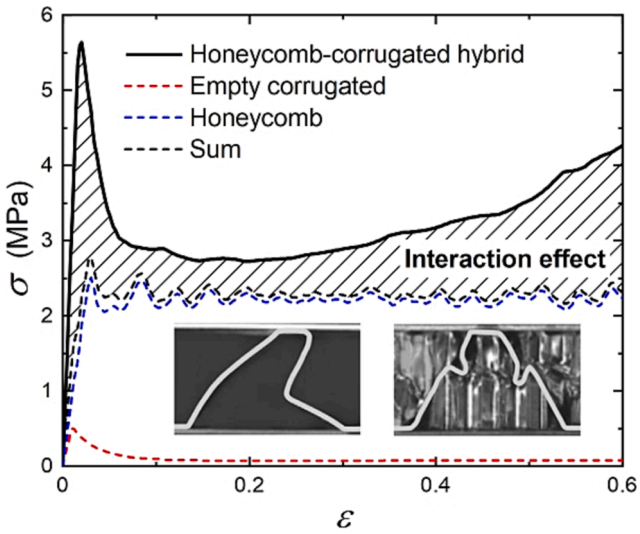

Fig. 1. Experimentally measured, quasi-static out-of-plane compressive stress versus strain curves of sandwiches having honeycomb, empty corrugated, and hybrid honeycomb-corrugated cores, together with typical deformation images of empty corrugated and hybrid cores captured at $\varepsilon = 0.25$ [18].

Built upon the somewhat disappointing foam-filling approach for all-metallic sandwich constructions, either because the foam fillers are too weak or too heavy, reduce the weight of the core, the present authors [17,18] proposed filling an all-metallic corrugated sandwich panel with metallic honeycomb blocks and systematically studied its quasi-static mechanical performance, both experimentally and numerically. We demonstrated that compared to a sandwich panel with either empty corrugated or honeycomb core having equal mass, the rigidity, strength, and energy absorption of the hybrid honeycomb-corrugated sandwich panel under out-of-plane compression, transverse shear, and three-point bending are all dramatically enhanced with minimal increase in structural mass. For instance, as shown in Fig. 1, under quasi-static out-of-plane compression, the experimentally measured flow stress of the proposed hybrid-core sandwich is significantly higher than that obtained from summing its constituent contributions, i.e., the curve 'Sum'. Further, the large shaded area between the curves of 'Honeycomb-corrugated hybrid' and 'Sum' in Fig. 1 implies the interaction (coupling) effect between honeycomb and corrugation is strong: while the honeycomb provides lateral support to the corrugated members, the corrugated members also strengthen the honeycomb; as a result, the crushing modes of both constituents at large plastic deformation are altered, as shown by the inserted images of Fig. 1. Subsequently, by introducing periodically distributed micro-perforations onto the incident face sheet as well as the corrugated members, it has also been demonstrated that the proposed honeycomb-corrugated sandwich construction also exhibits superior sound absorbing capability [19].

In addition to high rigidity/strength/energy absorption, the vibration characteristics of the proposed hybrid sandwich are also found to be significant. Zhang et al. [20] used both finite element (FE) simulation and experimental measurement to study the free vibration of a honeycomb-corrugated sandwich beam, after obtaining its equivalent parameters via a homogenization approach. Nonetheless, as will be demonstrated later in the current study, the unreasonable use of honeycomb equivalent stiffness and the neglect of honeycomb-corrugated interaction by Zhang et al. [20] led to large errors in the predicted high-order natural frequencies of the hybrid-cored sandwich beam. In addition to numerical simulation and experimental measurement, theoretical modeling of free vibration of honeycomb-corrugated sandwiches is rarely reported. Although the equivalent single layer theories (such as the classical laminate theory, the first-order shear deformation theory, the high-order deformation theories [21–23], etc.) and, more recently, the layer-wise theories [24–27] have been adopted to describe the displacement field of a sandwich structure, certain assumptions on stresses and strains must be introduced to eliminate the errors caused by ignoring the deformation in its thickness direction, thus leading to inaccurate predictions of frequency responses when the sandwich core is relatively thick. Since no assumptions are made about the deformation and stress of plates, the three-dimensional (3D) elasticity theory [28] is deemed more suitable for the analysis of sandwich plates with honeycomb-corrugated cores. For sandwich plates with complex cores (such as graded auxetic honeycomb core [29] and foam-filled composite corrugated core [30], etc.), an approach combining core homogenization and plate deformation theory is widely used to study the free vibration characteristics.

The present study aims to establish a theoretical model that combines the homogenization of sandwich core with the 3D elasticity theory to analyze the free vibration performance of sandwich plates with honeycomb-corrugated hybrid cores. Based on micromechanics analysis of representative volume element (RVE), the proposed model not only accounts for the effect of honeycomb-corrugated coupling but also presents accurate equivalent constitutive relations of hexagonal honeycombs that had been incorrectly expressed in previous studies. Upon validating the proposed theoretical model against 3D FE simulations, the model is employed to explore how mutual restraint between the constituents of the hybrid core suppresses local vibration of the sandwich structure, resulting in a higher frequency response than competing sandwich constructions of equal mass.

The paper is arranged as follows: In Section 2, the equivalent elastic constants of the honeycomb-corrugated hybrid core are obtained based on the homogenization method; in Section 3, the free vibration of the homogenized sandwich plate is analyzed based on the 3D elasticity theory; in Section 4, the accuracy and convergence of the equivalent parameters of honeycomb-corrugated hybrid core are verified by the FE model; in Section 5, the influence of the geometric parameters on the fundamental frequency of the honeycomb-corrugated sandwich plate is analyzed, the first three natural frequencies of the hybrid sandwich plate are compared with the traditional sandwich structures, and the effect of hybrid design on structure weight is studied. Finally, the conclusion of this study is given in Section 6.

2. Homogenization of honeycomb-corrugated hybrid core

Fig. 2(a) presents schematically the manufacturing process of an ultralightweight all-metallic sandwich plate with honeycomb-corrugated core. For a typical instance, the hybrid core is composed of corrugated thin aluminum (Al) plate and trapezoidal Al honeycomb blocks. For simplicity, the standard hexagonal honeycombs are considered, although honeycombs with different morphologies can also be used to construct the proposed hybrid core. The hexagonal honeycomb is manufactured using an expansion manufacturing process [31] (Fig. 2 (a): ①–③). Then, as shown in Fig. 2(a): ④, trapezoidal honeycomb blocks are precisely cut from the prepared honeycomb using electrical discharge machining (EDM). Subsequently, the corrugated plate (folded plate) is produced using the stamping method as depicted in Fig. 2(a): ⑤. Finally, as shown in Fig. 2(a): ⑥–⑦, the hybrid-cored sandwich plate is fabricated by inserting the trapezoidal honeycomb blocks into the corrugated plate, fixed by epoxy adhesive and then adhesively bonded to the Al face sheets. The aviation-grade epoxy adhesive Loctite® EA E-120HP is used for bonding and is required to solidify at room temperature for 36 h. Photograph of a typical sample fabricated via this route is presented in Fig. 2(b). Alternatively, the core and the face sheets can be bonded with brazing. For instance, if the corrugated core and the face sheets are both made of 304 stainless steel, then the corrugated sandwich can be first prepared by vacuum brazing using BNi-7 brazing alloy at a brazing temperature of 1040 °C and a vacuum atmosphere of 5×10^{-3} Pa [32,33]. Then, trapezoidal honeycomb blocks (say, made of Al) are inserted into the corrugated sandwich and glued with epoxy

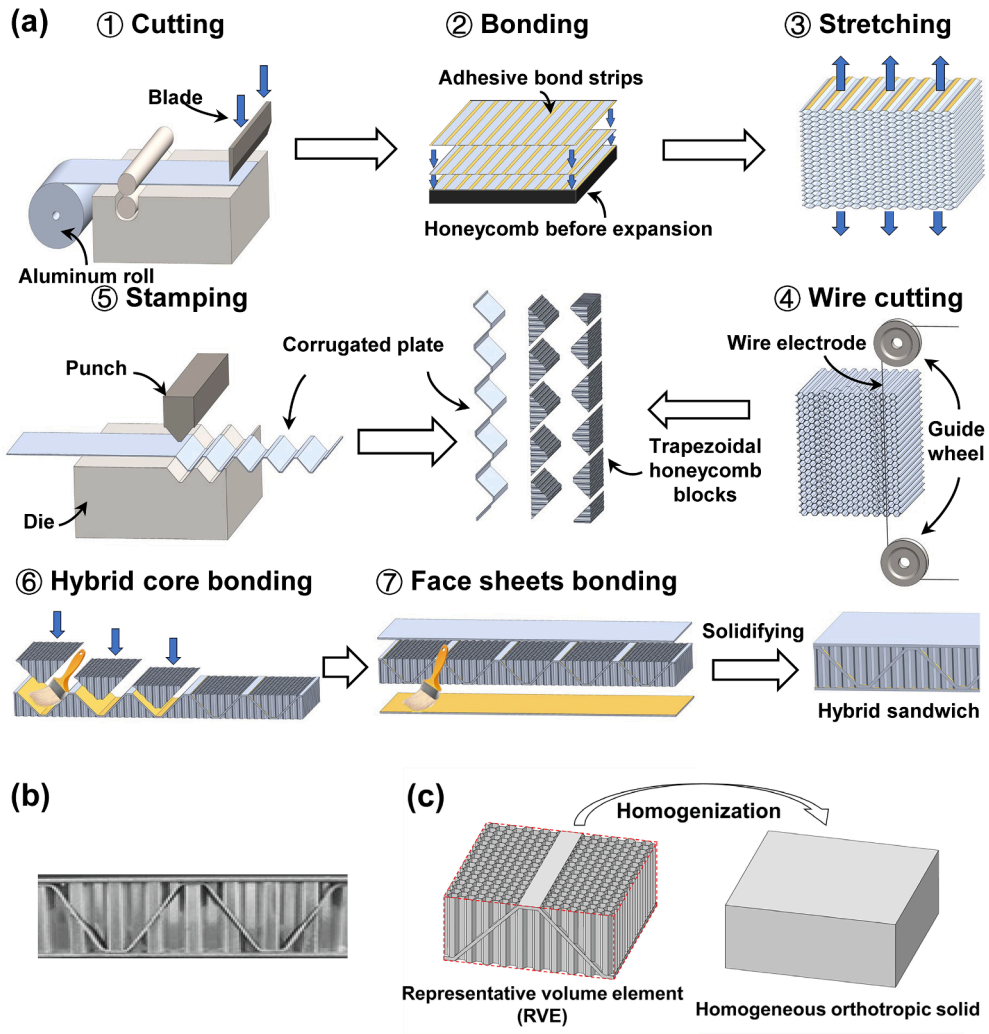

Fig. 2. (a) Schematic of manufacturing process for honeycomb-corrugated sandwich plate; (b) Photograph of as-fabricated sandwich sample; (c) Representative volume element (RVE) of hybrid core.

adhesive.

With either adhesive bonding or brazing, it has been established that the bonding strength between the face sheets and the core is sufficiently high, as FE simulations assuming perfect bonding agreed well with the experimentally measured dynamic response of hybrid-cored sandwich panel under impulsive loading [32,33].

To investigate theoretically the free vibration performance of the novel honeycomb-corrugated sandwich, the following assumptions are made: (1) the whole sandwich plate experiences linear small elastic deformation, and no local buckling occurs; (2) the size of honeycomb cell is much smaller than the macroscopic size of the sandwich; (3) the two face sheets are perfectly connected with the hybrid core, while the honeycomb cells are tightly connected with adjacent corrugated members and do not experience relative displacement under loading.

Based upon the foregoing assumptions, the honeycomb-corrugated hybrid core can be analyzed at two different scales: (a) at the macroscopic scale, the core is treated as a homogeneous orthotropic material, as illustrated in Fig. 2(c); (b) at the mesoscopic scale, contributions of the honeycomb and corrugation to the whole hybrid are separately considered, with their coupling effect duly accounted for.

Based on the method of homogenization, the *meso*-macro relationship of the hybrid core is obtained by analyzing its RVE, or unit cell, which is depicted in Fig. 2(c). Note that, in practice, to facilitate welding/gluing between face sheets and the core, a corrugated platform is commonly introduced, as shown in Fig. 2(c).

2.1. Geometric configuration

The geometric configuration and reference coordinate system of the RVE (i.e., unit cell) selected for the honeycomb-corrugated hybrid core is displayed in Fig. 3. The Cartesian coordinates x-y-z represent the global coordinates of the RVE, while the Cartesian coordinates X-Y-Z represent the local coordinates of the inclined corrugated plate. Relevant geometric parameters are: honeycomb wall length l_H, honeycomb wall thickness t_H, honeycomb cell angle Φ, corrugated length l_C, corrugated thickness t_C, corrugated angle θ, and width of corrugated platform d. Accordingly, the volume fractions of honeycomb and corrugated plate, λ_H and λ_C, can be separately expressed as [34]:

$$\lambda_H = \frac{2t_H}{(1-\cos\Phi)\sin\Phi l_H} \tag{1a}$$

$$\lambda_C = \frac{t_C(l_C+d)}{(t_C+l_C\sin\theta)(d+l_C\cos\theta)} \tag{1b}$$

Let E_H, ν_H, and ρ_H denote Young's modulus, Poisson ratio and mass density of the isotropic material make for the honeycomb. Let E_C, ν_C, and ρ_C denote the corresponding material properties of the corrugated plate. The mass density of the honeycomb-corrugated hybrid core is thence given by:

$$\rho_{core} = \rho_C\lambda_C + \rho_H\lambda_H(1-\lambda_C) \tag{2}$$

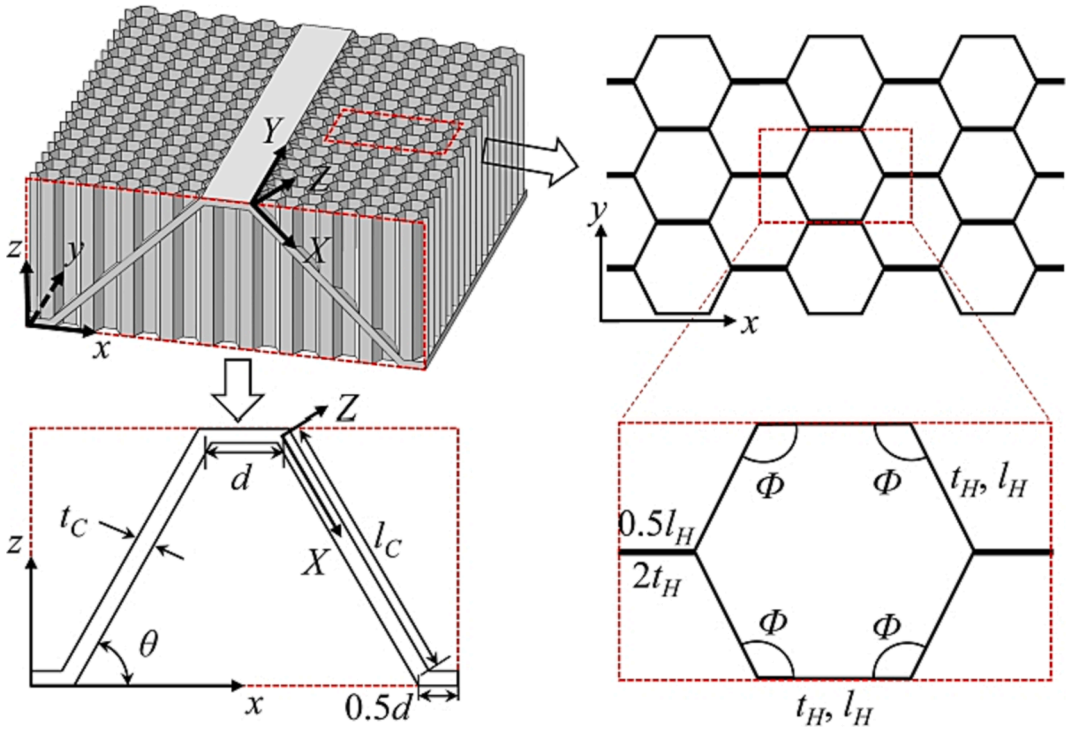

Fig. 3. Geometric configuration and reference coordinate system of the RVE.

2.2. Equivalent elastic constants of RVE

The macro-homogeneity equality of Hill [35] is adopted in the present study, which reads:

$$\Sigma\cdot\mathrm{E} = \langle\boldsymbol{\sigma}\cdot\boldsymbol{\varepsilon}\rangle_\Omega = \frac{1}{\Omega}\int_\Omega \boldsymbol{\sigma}\cdot\boldsymbol{\varepsilon}\, d\Omega \tag{3}$$

$$\mathrm{E} = \langle\boldsymbol{\varepsilon}\rangle_\Omega = \frac{1}{\Omega}\int_\Omega \boldsymbol{\varepsilon}\, d\Omega \tag{4}$$

$$\Sigma = \langle\boldsymbol{\sigma}\rangle_\Omega = \frac{1}{\Omega}\int_\Omega \boldsymbol{\sigma}\, d\Omega \tag{5}$$

where $\boldsymbol{\sigma}$ and $\boldsymbol{\varepsilon}$ denote the microscale stress tensor and the microscale strain tensor, $\boldsymbol{\Sigma}$ and $\mathbf{E}$ denote the macroscopic stress tensor and the macroscopic strain tensor, respectively, Ω represents the volume of the RVE, and $\langle\bullet\rangle_\Omega$ denotes volume averaging. Thus, $\boldsymbol{\Sigma}\cdot\mathbf{E}\boldsymbol{\Omega}$ is the macroscopic strain energy density and $\int_\Omega \boldsymbol{\sigma}\cdot\boldsymbol{\varepsilon}\, d\Omega$ is the total strain energy density of the admissible microscopic fields. Eq. (3) implies that the volume averaged strain energy density of an inhomogeneous material can be obtained by multiplying the separate volume averages of microscopic stresses and strains.

Consider next the case when the RVE produces a deformation shown in Fig. 4(a) under the uniform displacement boundary condition of $\mathbf{u} = \mathbf{E}\cdot\mathbf{x}$, where $\mathbf{x}$ represents the point on the boundary and $\mathbf{E}$ represents the macroscopic strain tensor in the x-z plane. For small deformations, it is assumed that a uniform strain field is generated inside the RVE under the displacement boundary condition. Thus, the macroscopic strain of the RVE and the microscopic strain of each of its constituents can be corresponded using a simple geometric relationship. For the sake of theoretical analysis, the influence of the corrugated platform on the equivalent elastic constants of the hybrid core is ignored, because the platform is taken as perfectly connected to the face sheet and hence its deformation is consistent with the latter. The corrugated member (i.e., the inclined plate) can be characterized as an Euler-Bernoulli beam of unit width along the y-direction, with both of its ends clamped [36].

Analogous to the analysis of pin-reinforced foam core and foam-filled corrugated core [30,37], the macroscopic strain energy density of the present honeycomb-corrugated core can be calculated as:

$$U = U_C + U_H \tag{6}$$

$$U_C = \frac{1}{\Omega}\sum_{i=1}^{2}\left[\frac{1}{2}(\mathbf{u}^{(i)} + 2\mathbf{u}_p^{(i)})^{\mathrm{T}}\mathbf{K}^{(i)}\mathbf{u}^{(i)}\right] \tag{7}$$

$$U_H = (1-\lambda_C)\left(\frac{1}{2}\Xi^{\mathrm{T}}\mathbf{C}^H\Xi\right) \tag{8}$$

$$\Xi = (\Xi_1,\ \Xi_2,\ \Xi_3,\ \Xi_4,\ \Xi_5,\ \Xi_6)^T = (E_{11},\ E_{22},\ E_{33},\ 2E_{23},\ 2E_{13},\ 2E_{12})^T \tag{9}$$

with.

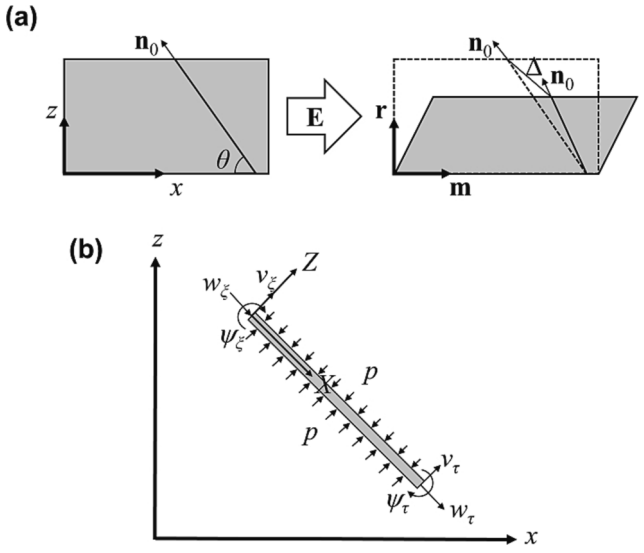

Fig. 4. (a) Deformation of RVE subjected to macroscopic strain $\mathbf{E}$, and (b) forces acting on corrugated member (inclined plate).

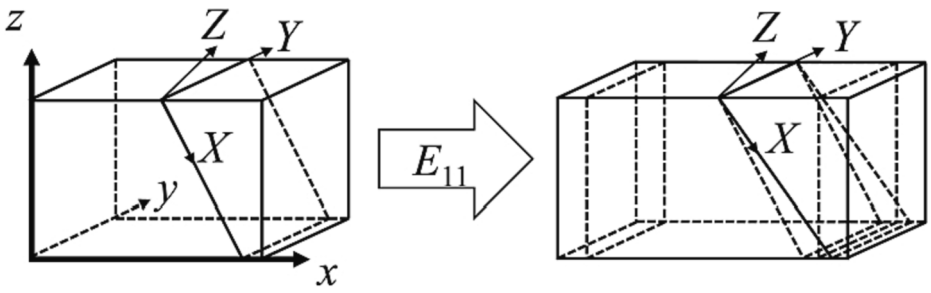

Fig. 5. Deformation of RVE subjected to macroscopic strain E_{11}.

$$\Omega = 2(l_C\cos\theta + d)(l_C\sin\theta + t_C) \tag{10}$$

Here, U_C and U_H are the macroscopic strain energy density of the corrugated and honeycomb, respectively; $\boldsymbol{\Xi}$ is the macroscopic strain vector; $\mathbf{C}^H$ is the stiffness matrix of the honeycomb; $\mathbf{u}^{(i)}$ is the global nodal displacement vector of the i-th inclined beam characterized by end nodes ξ and τ, as shown in Fig. 4(b):

$$\mathbf{u}^{(i)} = \mathbf{T}^{(i)\mathrm{T}}\mathbf{u}_e^{(i)} \tag{11}$$

$$\mathbf{u}_e^{(i)} = (w_\xi,\ v_\xi,\ \psi_\xi,\ w_\tau,\ v_\tau,\ \psi_\tau)^{(i)T} \tag{12}$$

where w, v, and ψ represent the displacement components of the end node in local coordinate plane X-Z. $\mathbf{T}^{(i)}$ is the transformation matrix between local and global coordinates for the i-th inclined beam, and its detailed expression is presented in Appendix B. For small deformations, the global nodal displacement $\boldsymbol{\Delta}$ is given by [36]:

$$\Delta = l_C\mathbf{E}\mathbf{n}_0 = (\Delta_1\mathbf{m},\ \Delta_2\mathbf{r}) \tag{13}$$

$$\mathbf{E} = \begin{bmatrix} E_{11} & E_{13} \\ sym & E_{33} \end{bmatrix} \tag{14}$$

where $\mathbf{n}_0$ denotes the unit vector along the inclined beam, Δ_1 and Δ_2 are projections of $\boldsymbol{\Delta}$ along with the x and z coordinates, and $\mathbf{m}$ and $\mathbf{r}$ represent unit vectors along the x and z coordinates, respectively. Then, $\mathbf{u}^{(i)}$ can be expressed as:

$$\mathbf{u}^{(i)} = (\Delta_1,\ \Delta_2,\ 0,\ 0,\ 0,\ 0)^{(i)\mathrm{T}} \tag{15}$$

In Eq. (4), $\mathbf{u}_p{}^{(i)}$ is the global nodal displacement vector of the i-th inclined beam induced by lateral normal stress $p^{(i)}$, as shown in Fig. 4(b). It represents the coupling effect between honeycomb and corrugated plate and can be expressed as:

$$\mathbf{u}_p^{(i)} = \mathbf{T}^{(i)\mathrm{T}}\mathbf{u}_{pe}^{(i)} \tag{16}$$

$$\mathbf{u}_{pe}^{(i)} = \left(\frac{v_C p^{(i)} l_C}{E_C/(1-v_C^2)},\ 0,\ 0,\ 0,\ 0,\ 0\right)^{(i)T} \tag{17}$$

where the influence of shear stress on the corrugated plate is ignored, and only elongation of the corrugated plate induced by lateral support of adjacent honeycomb blocks is considered. For simplicity, with $p^{(i)}$ taken as uniformly distributed on the lateral surface of the i-th inclined plate, it can be approximately calculated as:

$$p^{(i)} = \mathbf{n}_1^{(i)T}\begin{bmatrix} \sigma_{11} & \sigma_{12} & \sigma_{13} \\ \sigma_{21} & \sigma_{22} & \sigma_{23} \\ \sigma_{31} & \sigma_{32} & \sigma_{33} \end{bmatrix}^H \mathbf{n}_1^{(i)} \tag{18}$$

$$\boldsymbol{\sigma}^H = \mathbf{C}^H\Xi \tag{19}$$

where $\mathbf{n}_1^{(i)}$ is the unit vector normal to the lateral surface of the i-th corrugated plate.

In Eq. (4), $\mathbf{K}^{(i)}$ is the global stiffness matrix that satisfies the transformation between local and global coordinates, as:

$$\mathbf{K}^{(i)} = \mathbf{T}^{\mathrm{T}(i)}\mathbf{K}_e^{(i)}\mathbf{T}^{(i)} \tag{20}$$

where $\mathbf{K}_e{}^{(i)}$ is the elementary stiffness matrix of the i-th inclined beam, as given in Appendix B. It follows that the effective stiffness of the RVE in the x-z plane can be calculated as:

$$C_{ij} = \frac{\partial^2 U}{\partial\Xi_i\partial\Xi_j} \tag{21}$$

In the global x-z plane, the macroscopic equivalent stiffnesses of the honeycomb-corrugated hybrid core can thence be obtained as:

$$C_{11} = \frac{2E_C t_C l_C}{(1-v_C^2)\Omega}\cos^4\theta + \frac{E_C t_C^3}{2(1-v_C^2)l_C\Omega}\sin^2 2\theta + \frac{v_C t_C l_C}{\Omega}\left(C_{11}^H\sin^2 2\theta + 4C_{13}^H\cos^4\theta\right) + (1-\lambda_C)C_{11}^H \tag{22}$$

$$C_{13} = \frac{E_C t_C l_C}{2(1-v_C^2)\Omega}\sin^2 2\theta - \frac{E_C t_C^3}{2(1-v_C^2)l_C\Omega}\sin^2 2\theta + \frac{v_C t_C l_C}{\Omega}\left(2C_{11}^H\sin^4\theta + C_{13}^H\sin^2 2\theta + 2C_{33}^H\cos^4\theta\right) + (1-\lambda_C)C_{13}^H \tag{23}$$

$$C_{33} = \frac{2E_C t_C l_C}{(1-v_C^2)\Omega}\sin^4\theta + \frac{E_C t_C^3}{2(1-v_C^2)l_C\Omega}\sin^2 2\theta + \frac{v_C t_C l_C}{\Omega}\left(4C_{13}^H\sin^4\theta + C_{33}^H\sin^2 2\theta\right) + (1-\lambda_C)C_{33}^H \tag{24}$$

$$C_{55} = \frac{E_C t_C l_C}{2(1-v_C^2)\Omega}\sin^2 2\theta + \frac{E_C t_C^3}{2(1-v_C^2)l_C\Omega}\cos^2 2\theta - \frac{2v_C t_C l_C}{\Omega}C_{55}^H\sin^2 2\theta + (1-\lambda_C)C_{55}^H \tag{25}$$

If a macroscopic strain E_{11} (E_{22}, or E_{33}) is solely imposed on the RVE (Fig. 5), the equilibrium equation of macroscopic force and mesoscopic force in the y-direction can be expressed as:

$$C_{12}E_{11}\Omega = 2E_{11}\cos^2\theta\frac{E_C v_C}{1-v_C^2}t_C l_C + 2v_C p_1 t_C l_C + (1-\lambda_C)C_{12}^H E_{11}\Omega \tag{26}$$

$$C_{22}E_{22}\Omega = 2E_{22}\frac{E_C}{1-v_C^2}t_C l_C + 2v_C p_2 t_C l_C + (1-\lambda_C)C_{22}^H E_{22}\Omega \tag{27}$$

$$C_{23}E_{33}\Omega = 2E_{33}\sin^2\theta\frac{E_C v_C}{1-v_C^2}t_C l_C + 2v_C p_3 t_C l_C + (1-\lambda_C)C_{23}^H E_{33}\Omega \tag{28}$$

Here, the first and third terms on the right-hand side of the equilibrium equation represent the mesoscopic forces contributed by the corrugated plate and the honeycomb, respectively, and (p_1, p_2, p_3) represent the lateral normal stresses between honeycomb and corrugated plate. Using similar procedures to derive the lateral normal stress $p^{(i)}$, one arrives at:

$$p_j = \mathbf{n}_1^T\begin{bmatrix} \sigma_{11} & \sigma_{12} & \sigma_{13} \\ \sigma_{21} & \sigma_{22} & \sigma_{23} \\ \sigma_{31} & \sigma_{32} & \sigma_{33} \end{bmatrix}_j \mathbf{n}_1 \tag{29}$$

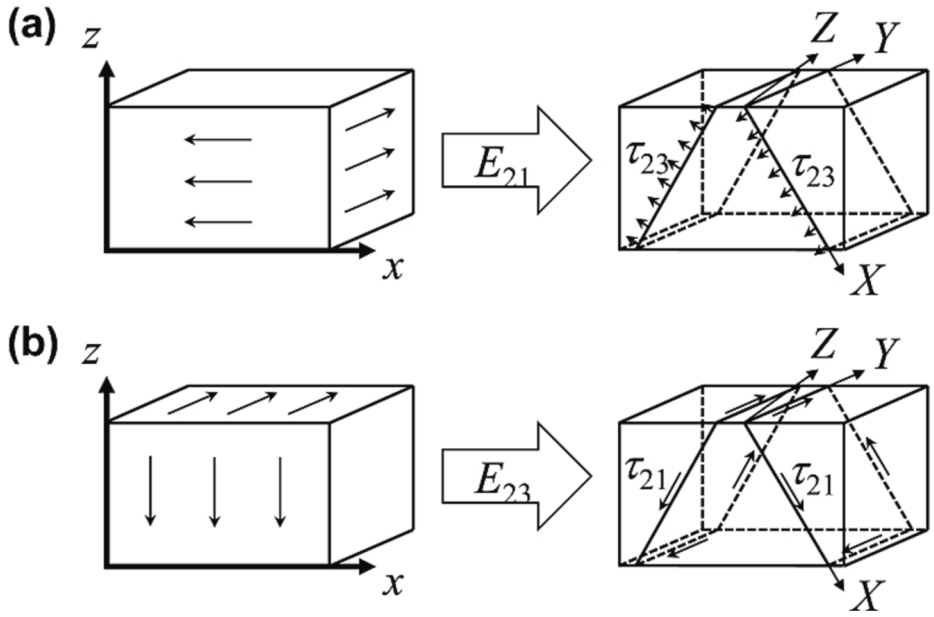

Fig. 6. (a) Shear flow of RVE subjected to macroscopic strain E_{21}, and (b) shear flow of RVE subjected to macroscopic strain E_{23}.

$$\boldsymbol{\sigma}_j = \begin{cases} \mathbf{C}^H(E_{11},\ 0,\ 0,\ 0,\ 0,\ 0)^T\ j=1 \\ \mathbf{C}^H(0,\ E_{22},\ 0,\ 0,\ 0,\ 0)^T\ j=2 \\ \mathbf{C}^H(0,\ 0,\ E_{33},\ 0,\ 0,\ 0)^T\ j=3 \end{cases} \tag{30}$$

When subjected to macroscopic shear strain E_{21} or E_{23}, the distributed shear flow in the RVE is shown in Fig. 6(a) or (b), in which cases the coupling effect of honeycomb and corrugation vanishes. Force balance of the RVE can be written as:

$$C_{44}2E_{23}\Omega = 2\tau_{21}t_C l_C \sin\theta + (1-\lambda_C)C_{44}^H 2E_{23}\Omega \tag{31}$$

$$C_{66}2E_{21}\Omega = 2\tau_{23}t_C l_C \sin\theta + (1-\lambda_C)C_{66}^H 2E_{12}\Omega \tag{32}$$

where the first and second terms on the right-hand side represent mesoscopic forces contributed by the corrugation and the honeycomb, respectively, and τ_{21} and τ_{23} represent separately shear stresses in local coordinates *X-Y-Z*. Correspondingly, the local shear strains are calculated as:

$$\varepsilon_{21} = \frac{\tau_{21}}{2G};\ \varepsilon_{23} = \frac{\tau_{23}}{2G};\ G = \frac{E_C}{2(1+v_C)} \tag{33}$$

where G is the shear modulus of the base material.

Finally, the remaining macroscopic equivalent stiffnesses related to the global *y*-coordinate are obtained as:

$$C_{12} = \frac{2E_C v_C t_C l_C}{(1-v_C^2)\Omega}\cos^2\theta + \frac{2v_C t_C l_C}{\Omega}\left(\sin^2\theta C_{11}^H + \cos^2\theta C_{13}^H\right) + (1-\lambda_C)C_{12}^H \tag{34}$$

$$C_{22} = \frac{2E_C t_C l_C}{(1-v_C^2)\Omega} + \frac{2v_C t_C l_C}{\Omega}\left(\sin^2\theta C_{12}^H + \cos^2\theta C_{23}^H\right) + (1-\lambda_C)C_{22}^H \tag{35}$$

$$C_{23} = \frac{2E_C v_C t_C l_C}{(1-v_C^2)\Omega}\sin^2\theta + \frac{2v_C t_C l_C}{\Omega}\left(\sin^2\theta C_{13}^H + \cos^2\theta C_{33}^H\right) + (1-\lambda_C)C_{23}^H \tag{36}$$

$$C_{44} = \frac{E_C t_C l_C}{(1+v_C)\Omega}\sin^2\theta + (1-\lambda_C)C_{44}^H \tag{37}$$

$$C_{66} = \frac{E_C t_C l_C}{(1+v_C)\Omega}\sin^2\theta + (1-\lambda_C)C_{66}^H \tag{38}$$

It should be pointed out that the stiffness matrix of hexagonal honeycomb presented in a previous study [20] is somewhat inaccurate. In the following section, the correct stiffness matrix is derived.

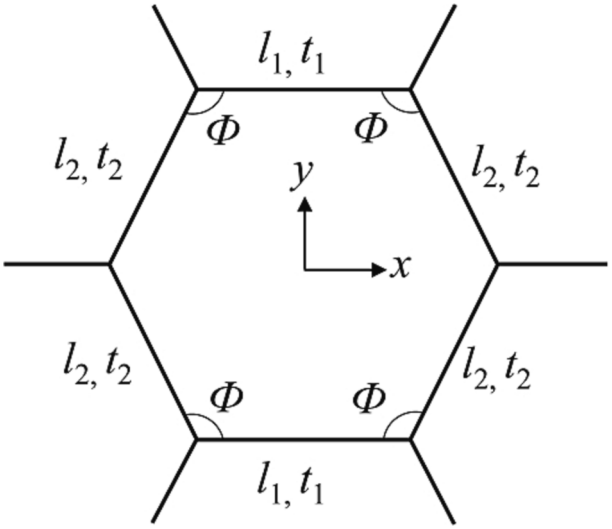

Fig. 7. Geometric parameters of hexagonal honeycomb in Ref. [20].

2.3. Stiffness matrix of hexagonal honeycomb

In a honeycomb-corrugated sandwich plate, the inserted honeycomb blocks mainly play the role of supporting the face sheets and corrugated members and have a relatively small contribution to the bending stiffness of the sandwich. However, if honeycomb stiffness is not determined correctly, the accuracy of subsequent free vibration analysis of the hybrid-cored sandwich is in doubt.

Fig. 7 displays the geometry of the hexagonal honeycomb described in a previous free vibration study of the hybrid-cored sandwich beam [20]. Let the length and thickness of the horizontal cell wall be denoted by l_1 and t_1, and the length and thickness of the inclined cell wall by l_2 and t_2, respectively. For the hexagonal honeycomb of concern, $l_1 = l_2$ and $t_1 = 2\ t_2$. In Ref. [20], the elastic constants of the inserted honeycomb were derived based on the honeycomb stiffness matrix presented in Hohe et al. [38]. When the geometry of the honeycomb is set to $l_1 = 1$ mm, $t_1 = 0.12$ mm, $\Phi = 120°$, and the material properties are set to $E_H =$

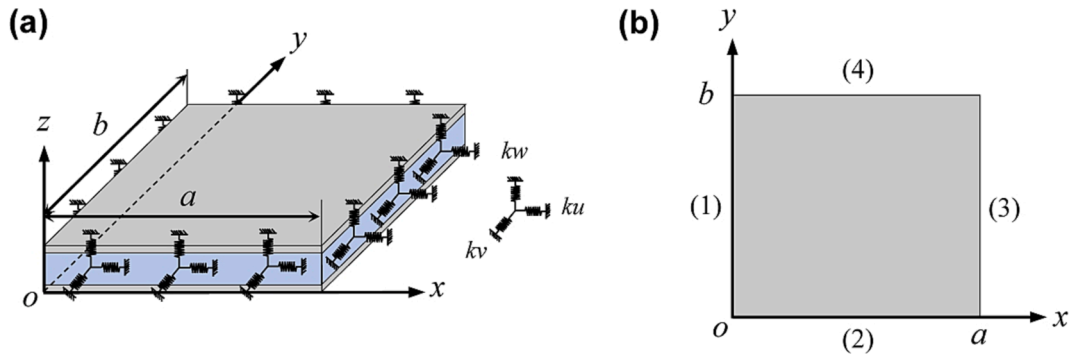

Fig. 8. (a) Sandwich plate with homogenized hybrid core and reference Cartesian coordinate system, and (b) labels for each edge.

70 GPa and $v_H = 0.3$, its stiffness matrix is calculated as:

$$\boldsymbol{C}^H = \begin{bmatrix} 0.3387 & 1.2074 & 0 & 0 & 0 & 0 \\ & 1.2175 & 0 & 0 & 0 & 0 \\ & & 6.4663 & 0 & 0 & 0 \\ & & & 0.9326 & 0 & 0 \\ & sym & & & 0.5829 & 0 \\ & & & & & 50518 \end{bmatrix} \text{GPa} \tag{39}$$

Nonetheless, without changing the above settings of geometrical and material parameters, the stiffness matrix of the hexagonal honeycomb derived according to the formulas presented by Shi et al. [39] is calculated:

$$\boldsymbol{C}^H = \begin{bmatrix} 1.4631 & 1.4514 & 0 & 0 & 0 & 0 \\ & 1.4573 & 0 & 0 & 0 & 0 \\ & & 6.4663 & 0 & 0 & 0 \\ & & & 0.9326 & 0 & 0 \\ & sym & & & 1.3990 & 0 \\ & & & & & 0.0256 \end{bmatrix} \text{GPa} \tag{40}$$

which exhibits significant differences from the stiffness matrix given by Ref. [20]. By comparing the corresponding equivalent stiffness expressions in the three existing studies, namely, Refs. [20,38,39], it is established that the discrepancies are mainly attributed to two causes:

(1) The formula expression for γ_1 presented in Hohe et al. [38] exhibits a clerical error, which was inherited by Zhang et al. [20] in their analysis of hybrid-cored sandwich beams, as:

$$\gamma_1 = 1 + 2\frac{t_2^2}{l_2^2}\cos^3\Phi + 2\frac{t_2^3}{t_1 l_2^2 \gamma}\sin\Phi\cos\Phi \tag{41}$$

The correct expression of γ_1 derived according to Shi et al. [39] is:

$$\gamma_1 = 1 + 2\frac{t_2}{t_1}\cos^3\Phi + 2\frac{t_2^3}{t_1 l_2^2 \gamma}\sin\Phi\cos\Phi \tag{42}$$

(2) In addition to inheriting the clerical error from [38], the elastic constants of honeycomb in Ref. [20] contain additional clerical errors. For example, in equation of C_{11}^H, the denominator is incorrectly magnified 6 times, which makes C_{11}^H extremely small; in equation of C_{22}^H, the minus sign in the numerator is changed to a plus sign; in equation of C_{66}^H, β_6 in the denominator is missing, which makes C_{66}^H extremely large.

Finally, based upon the equivalent constitutive equations derived by Shi et al. [39] using a two-scale method, the correct stiffness matrix of the hexagonal honeycomb shown in Fig. 7 is obtained as follows:

$$\boldsymbol{C}^H = \begin{bmatrix} C_{11}^H & C_{12}^H & 0 & 0 & 0 & 0 \\ & C_{22}^H & 0 & 0 & 0 & 0 \\ & & C_{33}^H & 0 & 0 & 0 \\ & & & C_{44}^H & 0 & 0 \\ & sym & & & C_{55}^H & 0 \\ & & & & & C_{66}^H \end{bmatrix} \tag{43}$$

$$C_{11}^H = E_H \frac{t_1 l_1 \left(1 - \frac{\gamma_1}{\beta}\right) - 2t_2 l_2 \left(\frac{l_1\gamma_1}{l_2\beta} - \cos\Phi\right)\cos^3\Phi}{2l_2(l_1 - l_2\cos\Phi)sin\Phi} \tag{44}$$

$$C_{12}^H = E_H \frac{-t_2\left(\frac{l_1\gamma_1}{l_2\beta} - \cos\Phi\right)\sin\Phi\cos\Phi}{l_1 - l_2\cos\Phi} \tag{45}$$

$$C_{22}^H = E_H \frac{t_2\left(\sin^2\Phi - \frac{l_1\gamma_2}{l_2\beta}cos\Phi\right)\sin\Phi}{l_1 - l_2\cos\Phi} \tag{46}$$

$$C_{33}^H = E_H \frac{l_1 t_1 + 2l_2 t_2}{2l_2(l_1 - l_2\cos\Phi)\sin\Phi} \tag{47}$$

$$C_{44}^H = G_H \frac{t_2\sin\Phi}{l_1 - l_2\cos\Phi} \tag{48}$$

$$C_{55}^H = G_H \frac{t_1 l_1 + 2t_2 l_2\cos^2\Phi - \frac{t_1 l_2 + 2t_2 l_2\cos\Phi}{t_1 l_2 + 2t_2 l_1}(t_1 l_1 + 2l_2 t_2\cos\Phi)}{2l_2(l_1 - l_2\cos\Phi)\sin\Phi} \tag{49}$$

$$C_{66}^H = \frac{E_H\left(l_1 - l_2\cos\Phi + l_1\sin^2\Phi\right)\left(1 - \frac{l_2}{l_1}\cos\Phi + \frac{l_1\cos\Phi}{l_2\gamma_6} - \frac{2\cos^2\Phi}{\gamma_6}\right)}{2l_2\sin\Phi(l_1 - l_2\cos\Phi)\beta_6} \tag{50}$$

$$\gamma = 1 + 2(1 + v_H)\frac{t_2^2}{l_2^2} \tag{51}$$

$$\gamma_1 = 1 + 2\frac{t_2}{t_1}\cos^3\Phi + 2\frac{t_2^3}{t_1 l_2^2 \gamma}\sin\Phi\cos\Phi \tag{52}$$

$$\gamma_2 = 2\frac{t_2}{t_1}(\sin\Phi - \frac{t_2^2}{l_2^2\gamma})\sin\Phi\cos\Phi \tag{53}$$

$$\gamma_6 = 1 - \frac{l_1}{l_2}\cos\Phi \tag{54}$$

$$\beta = 1 + 2\frac{t_2 l_1}{t_1 l_2}\cos^2\Phi + 2\frac{l_1 t_2^3\sin^2\Phi}{t_1 l_2^3(1 - v_H^2)\gamma} \tag{55}$$

$$\beta_6 = \frac{l_1^2}{2t_1^3\gamma_6}(2 + \frac{t_1^3 l_2}{t_2^3 l_1}) + 2\frac{1 + v_H}{t_1\gamma_6}(\gamma_6 + \frac{l_1 t_1}{2l_2 t_2} + \frac{l_1}{l_2}\cos\Phi) + \frac{l_2\gamma_6}{2(1 - v_H^2)l_1 t_2\sin^2\Phi} \tag{56}$$

Eqs. (44)–(56) are employed in the present study to analyze the free vibration of honeycomb-corrugated sandwich plates.

3. Mathematical formulations for free vibration analysis

For the sandwich plate of concern, the hybrid core is taken as an equivalent homogeneous orthotropic material, and the face sheets are assumed made of a homogeneous isotropic material. The original honeycomb-corrugated sandwich plate then becomes a sandwich plate with a homogenized hybrid core or, equivalently, a three-layer laminate, as shown in Fig. 8(a). The Cartesian coordinate system *x-y-z* (consistent with global coordinates in Section 2) is used for analysis. Let *u*, *v*, and *w* represent the displacement components of the sandwich in *x*, *y*, and *z* directions, respectively. Three sets of independent springs (denoted herein by *ku*, *kv*, and *kw*) are introduced to the edges of the plate to achieve arbitrary adjustment of boundary conditions. For example, the classical clamped or free boundary can be modeled by setting the related spring stiffness to approach infinity or zero. To avoid ambiguity, the 4 edges of the sandwich are marked as (1), (2), (3), and (4) counter-clockwise, as shown in Fig. 8(b). Meanwhile, in subsequent derivation and analysis, the boundary conditions of each edge are also expressed in this order.

3.1. Constitutive laws and kinematic relations

For linear elastic deformation, the 3D elastic constitutive relation of face sheet material can be written as:

$$\begin{Bmatrix}\sigma_{xx}\\ \sigma_{yy}\\ \sigma_{zz}\\ \sigma_{xy}\\ \sigma_{xz}\\ \sigma_{yz}\end{Bmatrix}^{(i)} = \begin{bmatrix} A & B & B & 0 & 0 & 0 \\ & A & B & 0 & 0 & 0 \\ & & A & 0 & 0 & 0 \\ & & & C & 0 & 0 \\ & sym & & & C & 0 \\ & & & & & C \end{bmatrix}^{(i)} \begin{Bmatrix}\varepsilon_{xx}\\ \varepsilon_{yy}\\ \varepsilon_{zz}\\ \gamma_{xy}\\ \gamma_{xz}\\ \gamma_{yz}\end{Bmatrix}^{(i)} \tag{57}$$

where superscript $i = 1$ and 3 represent the lower face sheet and the upper face sheet, respectively, and the stiffness coefficients are given by:

$$A = \frac{E_f v_f}{(1+v_f)(1-2v_f)} + \frac{E_f}{1+v_f};$$
$$B = \frac{E_f v_f}{(1+v_f)(1-2v_f)}; \tag{58}$$
$$C = \frac{E_f}{2(1+v_f)}$$

Here, E_f, v_f, and ρ_f are Young's modulus, Poisson ratio, and mass density of face sheet material.

With the equivalent stiffnesses of the hybrid core derived in Section 2, its 3D elastic constitutive relation can be expressed as:

$$\begin{Bmatrix}\sigma_{xx}\\ \sigma_{yy}\\ \sigma_{zz}\\ \sigma_{yz}\\ \sigma_{xz}\\ \sigma_{xy}\end{Bmatrix}^{(i)} = \begin{bmatrix} C_{11} & C_{12} & C_{13} & 0 & 0 & 0 \\ & C_{22} & C_{23} & 0 & 0 & 0 \\ & & C_{33} & 0 & 0 & 0 \\ & & & C_{44} & 0 & 0 \\ & sym & & & C_{55} & 0 \\ & & & & & C_{66} \end{bmatrix}^{(i)} \begin{Bmatrix}\varepsilon_{xx}\\ \varepsilon_{yy}\\ \varepsilon_{zz}\\ \gamma_{yz}\\ \gamma_{xz}\\ \gamma_{xy}\end{Bmatrix}^{(i)} \tag{59}$$

where superscript $i = 2$ represent the hybrid core layer. In Appendix C , reasons for adopting the 3D formulation in the current study are further explained.

According to the linear, small-strain elasticity theory, the strain components are defined using the displacement *u*, *v*, and *w*, as:

$$\varepsilon_{xx} = \frac{\partial u}{\partial x};\ \varepsilon_{yy} = \frac{\partial v}{\partial y};\ \varepsilon_{zz} = \frac{\partial w}{\partial z};$$
$$\gamma_{xy} = \frac{\partial u}{\partial y} + \frac{\partial v}{\partial x};\ \gamma_{xz} = \frac{\partial u}{\partial z} + \frac{\partial w}{\partial x};\ \gamma_{yz} = \frac{\partial v}{\partial z} + \frac{\partial w}{\partial y} \tag{60}$$

3.2. Energy expressions

The strain energy U_e of the sandwich plate is given by:

$$U_e = \frac{1}{2}\sum_{i=1}^{3}\int_{V^{(i)}} (\sigma_{xx}^{(i)}\varepsilon_{xx} + \sigma_{yy}^{(i)}\varepsilon_{yy} + \sigma_{zz}^{(i)}\varepsilon_{zz} + \sigma_{yz}^{(i)}\gamma_{yz} + \sigma_{xz}^{(i)}\gamma_{xz} + \sigma_{xy}^{(i)}\gamma_{xy})dV^{(i)} \tag{61}$$

where $V^{(i)}$ is the volume of the *i*-th layer of the sandwich plate. Substituting Eqs. (57), (59), and (60) into Eq. (61) leads to:

$$\begin{aligned} U_e = \frac{1}{2}\int_0^a\int_0^b \Bigg\{ & \int_0^{t_{f1}} A\left[\left(\frac{\partial u}{\partial x}\right)^2 + \left(\frac{\partial v}{\partial y}\right)^2 + \left(\frac{\partial w}{\partial z}\right)^2\right] + 2B\left(\frac{\partial u}{\partial x}\frac{\partial v}{\partial y} + \frac{\partial u}{\partial x}\frac{\partial w}{\partial z}\right. \\ & \left. + \frac{\partial v}{\partial y}\frac{\partial w}{\partial z}\right) + C\left[\left(\frac{\partial u}{\partial y}\right)^2 + \left(\frac{\partial v}{\partial x}\right)^2 + \left(\frac{\partial u}{\partial z}\right)^2 + \left(\frac{\partial w}{\partial x}\right)^2 + \left(\frac{\partial v}{\partial z}\right)^2\right. \\ & \left. + \left(\frac{\partial w}{\partial y}\right)^2\right] + 2C\left(\frac{\partial u}{\partial y}\frac{\partial v}{\partial x} + \frac{\partial u}{\partial z}\frac{\partial w}{\partial x} + \frac{\partial v}{\partial z}\frac{\partial w}{\partial y}\right)dz + \int_{t_{f1}}^{t_{f1}+t_{core}} C_{11}\left(\frac{\partial u}{\partial x}\right)^2 \\ & + C_{22}\left(\frac{\partial v}{\partial y}\right)^2 + C_{33}\left(\frac{\partial w}{\partial z}\right)^2 + 2\left(C_{12}\frac{\partial u}{\partial x}\frac{\partial v}{\partial y} + C_{13}\frac{\partial u}{\partial x}\frac{\partial w}{\partial z} + C_{23}\frac{\partial v}{\partial y}\frac{\partial w}{\partial z}\right) \\ & + C_{66}\left[\left(\frac{\partial u}{\partial y}\right)^2 + \left(\frac{\partial v}{\partial x}\right)^2\right] + C_{55}\left[\left(\frac{\partial u}{\partial z}\right)^2 + \left(\frac{\partial w}{\partial x}\right)^2\right] + C_{44}\left[\left(\frac{\partial v}{\partial z}\right)^2\right. \\ & \left. + \left(\frac{\partial w}{\partial y}\right)^2\right] + 2\left(C_{66}\frac{\partial u}{\partial y}\frac{\partial v}{\partial x} + C_{55}\frac{\partial u}{\partial z}\frac{\partial w}{\partial x} + C_{44}\frac{\partial v}{\partial z}\frac{\partial w}{\partial y}\right)dz \\ & + \int_{t_{f1}+t_{core}}^{h} A\left[\left(\frac{\partial u}{\partial x}\right)^2 + \left(\frac{\partial v}{\partial y}\right)^2 + \left(\frac{\partial w}{\partial z}\right)^2\right] + 2B\left(\frac{\partial u}{\partial x}\frac{\partial v}{\partial y} + \frac{\partial u}{\partial x}\frac{\partial w}{\partial z}\right. \\ & \left. + \frac{\partial v}{\partial y}\frac{\partial w}{\partial z}\right) + C\left[\left(\frac{\partial u}{\partial y}\right)^2 + \left(\frac{\partial v}{\partial x}\right)^2 + \left(\frac{\partial u}{\partial z}\right)^2 + \left(\frac{\partial w}{\partial x}\right)^2 + \left(\frac{\partial v}{\partial z}\right)^2\right. \\ & \left. + \left(\frac{\partial w}{\partial y}\right)^2\right] + 2C\left(\frac{\partial u}{\partial y}\frac{\partial v}{\partial x} + \frac{\partial u}{\partial z}\frac{\partial w}{\partial x} + \frac{\partial v}{\partial z}\frac{\partial w}{\partial y}\right)dz \Bigg\} dxdy \end{aligned} \tag{62}$$

where $h = t_{f1} + t_{core} + t_{f3}$ represents the total thickness of the sandwich plate, t_{f1} and t_{f3} represent the thickness of the lower face sheet and the upper face sheet, respectively, and t_{core} is the thickness of the hybrid core.

The elastic potential energy stored in the springs of the sandwich plate boundary can be expressed as:

$$\begin{aligned} U_{spring} = & \frac{1}{2}\int_0^h\int_0^b \left[(ku_{x0} + ku_{xa})u^2 + (kv_{x0} + kv_{xa})v^2 + (kw_{x0} + kw_{xa})w^2\right]dydz \\ & + \frac{1}{2}\int_0^h\int_0^a \left[\left(ku_{y0} + ku_{yb}\right)u^2 + \left(kv_{y0} + kv_{yb}\right)v^2 + \left(kw_{y0}\right.\right. \\ & \left.\left. + kw_{yb}\right)w^2\right]dxdz \end{aligned} \tag{63}$$

where the subscripts *x*0, *xa*, *y*0, and *yb* indicate the positions of the springs. For example, *x*0 and *xa* indicate that the springs are distributed along the edge $x = 0$ and edge $x = a$, respectively.

The kinetic energy *T* of the sandwich plate is given by:

$$T = \frac{1}{2}\sum_{i=1}^{3}\int_{V^{(i)}} \rho^{(i)}\left(\left(\frac{\partial u}{\partial t}\right)^2 + \left(\frac{\partial v}{\partial t}\right)^2 + \left(\frac{\partial w}{\partial t}\right)^2\right)dV^{(i)} \tag{64}$$

where $\rho^{(i)}$ is the mass density of the *i*-th layer of the sandwich, with $\rho^{(i)} = \rho_f$ when $i = 1$ and 3 and $\rho^{(i)} = \rho_{core}$ when $i = 2$.

3.3. Admissible displacement functions and solution procedure

To avoid the potential discontinuity of the first-order displacement derivative at the edge of the sandwich plate, modified 3D Fourier cosine series supplemented with closed-form auxiliary functions are selected as the displacement functions that satisfy arbitrary boundary conditions, namely [28]:

$$u(x,y,z,t)=\left[\sum_{m=0}^{\infty}\sum_{n=0}^{\infty}\sum_{l=0}^{\infty}A_{mnl}\cos(\lambda_m x)\cos(\lambda_n y)\cos(\lambda_l z)+\sum_{m=0}^{\infty}\sum_{n=0}^{\infty}\times\sum_{k=1}^{2}a_{mnk}\cos(\lambda_m x)\cos(\lambda_n y)\xi_{kz}(z)+\sum_{m=0}^{\infty}\sum_{k=1}^{2}\times\sum_{l=0}^{\infty}a_{mkl}\cos(\lambda_m x)\xi_{ky}(y)\cos(\lambda_l z)+\sum_{k=1}^{2}\sum_{n=0}^{\infty}\times\sum_{l=0}^{\infty}a_{knl}\xi_{kx}(x)\cos(\lambda_n y)\cos(\lambda_l z)\right]e^{i\omega t} \tag{65}$$

$$v(x,y,z,t)=\left[\sum_{m\ =\ 0}^{\infty}\sum_{n=0}^{\infty}\sum_{l=0}^{\infty}B_{mnl}\cos(\lambda_m x)\cos(\lambda_n y)\cos(\lambda_l z)+\sum_{m=0}^{\infty}\sum_{n=0}^{\infty}\times\sum_{k=1}^{2}b_{mnk}\cos(\lambda_m x)\cos(\lambda_n y)\xi_{kz}(z)+\sum_{m=0}^{\infty}\sum_{k=1}^{2}\times\sum_{l=0}^{\infty}b_{mkl}\cos(\lambda_m x)\xi_{ky}(y)\cos(\lambda_l z)+\sum_{k=1}^{2}\sum_{n=0}^{\infty}\times\sum_{l=0}^{\infty}b_{knl}\xi_{kx}(x)\cos(\lambda_n y)\cos(\lambda_l z)\right]e^{i\omega t} \tag{66}$$

$$w(x,y,z,t)=\left[\sum_{m=0}^{\infty}\sum_{n=0}^{\infty}\sum_{l=0}^{\infty}C_{mnl}\cos(\lambda_m x)\cos(\lambda_n y)\cos(\lambda_l z)+\sum_{m=0}^{\infty}\sum_{n=0}^{\infty}\times\sum_{k=1}^{2}c_{mnk}\cos(\lambda_m x)\cos(\lambda_n y)\xi_{kz}(z)+\sum_{m=0}^{\infty}\sum_{k=1}^{2}\times\sum_{l=0}^{\infty}c_{mkl}\cos(\lambda_m x)\xi_{ky}(y)\cos(\lambda_l z)+\sum_{k=1}^{2}\sum_{n=0}^{\infty}\times\sum_{l=0}^{\infty}c_{knl}\xi_{kx}(x)\cos(\lambda_n y)\cos(\lambda_l z)\right]e^{i\omega t} \tag{67}$$

where A_{mnl}, B_{mnl}, C_{mnl}, a_{mnk}, b_{mnk}, c_{mnk}, a_{mkl}, b_{mkl}, c_{mkl}, a_{knl}, b_{knl}, and c_{knl} are unknown coefficients, ω is the natural frequency of the sandwich plate, i is the imaginary unit, and t is the time. The closed-form auxiliary functions are given as:

$$\xi_{kx}(x)=\begin{cases}x(\frac{x}{a}-1)^2 & k=1\\ \frac{x^2}{a}(\frac{x}{a}-1) & k=2\end{cases} \tag{68}$$

$$\xi_{ky}(y)=\begin{cases}y(\frac{y}{b}-1)^2 & k=1\\ \frac{y^2}{b}(\frac{y}{b}-1) & k=2\end{cases} \tag{69}$$

$$\xi_{kz}(z)=\begin{cases}z(\frac{z}{h}-1)^2 & k=1\\ \frac{z^2}{h}(\frac{z}{h}-1) & k=2\end{cases} \tag{70}$$

Based on the Rayleigh-Ritz method, the Lagrangian function of the sandwich plate system can be expressed as:

$$L=T-U_e-U_{spring} \tag{71}$$

where the strain energy of sandwich plate U_e, the potential energy of springs U_{spring}, and the kinetic energy T have been defined in Eqs. (62), (63), and (64), respectively. Substituting the three equations into (71) and minimizing the Lagrangian function against all unknown coefficients yields:

$$\frac{\partial L}{\partial \eta}=0;\quad \eta=A_{mnl},a_{mnk},a_{mkl},a_{knl},B_{mnl},b_{mnk},b_{mkl},b_{knl},C_{mnl},c_{mnk},c_{mkl},c_{knl} \tag{72}$$

Finally, the free vibration problem of the hybrid-cored sandwich plate having arbitrary boundary conditions is transformed into a standard eigenvalue problem, with the following governing equation obtained:

$$([K]+[K_S]-\omega^2[M])\{\Theta\}=\{0\} \tag{73}$$

where $[K]$ is the symmetric stiffness matrix obtained from the strain energy of the sandwich plate, $[K_S]$ is the stiffness matrix obtained from the potential energy of the springs, $[M]$ is the mass matrix, and Θ is the column vector of unknown coefficients.

4. Verification of equivalent elastic properties

To check the accuracy of equivalent elastic properties derived from the present theoretical method, a FE model of the RVE was established for the proposed honeycomb-corrugated sandwich to calculate its equivalent elastic properties, with periodic boundary conditions applied, as shown in Fig. 9. For the macroscopic strains E_{11}, E_{22}, and E_{33},

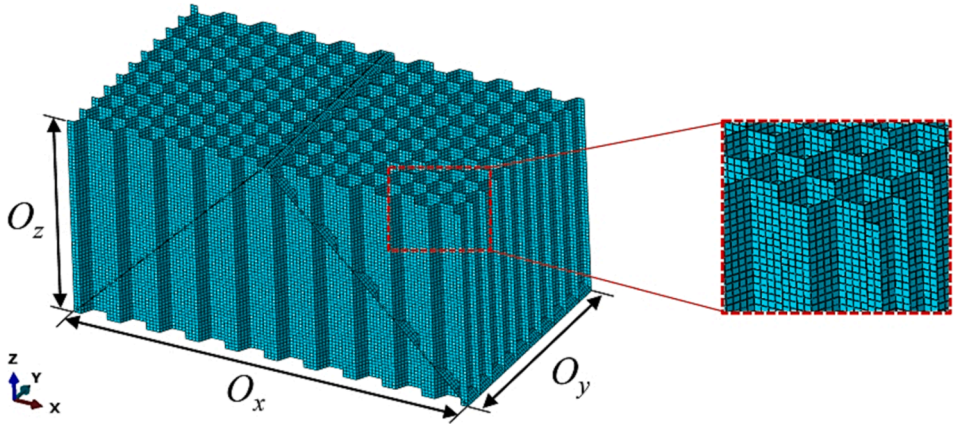

Fig. 9. FE model of the RVE.

Table 1
Geometric dimensions of the RVE.

t_H	l_H	Φ	t_C	θ	d	O_x	O_y	O_z
0.1 mm	1 mm	120°	0.5 mm	45°	0 mm	30 mm	17.32 mm	15 mm

the boundary conditions can be expressed as [40]:

$$\begin{aligned} &u_{x+} - u_{x-} = u_x; \quad u_x = E_{11}\cdot O_x; \\ &u_{y+,z+} = u_{y-,z-}; \\ &v_{x+,y+,z+} = v_{x-,y-,z-}; \\ &w_{x+,y+,z+} = w_{x-,y-,z-} \end{aligned} \tag{74}$$

$$\begin{aligned} &v_{y+} - v_{y-} = v_y; v_y = E_{22}\cdot O_y; \\ &u_{x+,y+,z+} = u_{x+,y-,z-}; \\ &v_{x+,z+} = v_{x-,z-}; \\ &w_{x+,y+,z+} = w_{x-,y-,z-} \end{aligned} \tag{75}$$

$$\begin{aligned} &w_{z+} - w_{z-} = w_z; \ w_z = E_{33}\cdot O_z; \\ &u_{x+,y+,z+} = u_{x-,y-,z-}; \\ &v_{x+,y+,z+} = v_{x-,y-,z-}; \\ &w_{x+,y+} = w_{x-,y-} \end{aligned} \tag{76}$$

where u, v, and w are the displacement components of the RVE along x, y, and z directions (Fig. 9), respectively. The subscript $x+$ and $x-$ represent nodes on the two boundaries perpendicular to the x-axis. O_x, O_y, and O_z are separately the length, width, and height of the RVE. Similarly, boundary conditions for the other macroscopic strains (i.e., E_{12}, E_{13}, E_{23}) can also be obtained, but not presented here for brevity.

As shown in Fig. 9, the FE model is established using shell element (linear quadrilateral element S4R in ABAQUS nomenclature), with at least 4 grids divided along honeycomb wall length to ensure the accuracy of calculation. Geometric dimensions of the RVE are listed in Table 1 and the base material properties (Al) are: Young's modulus 70 GPa, Poisson ratio 0.3, and mass density 2700 kg/m^3. The nodal force and nodal displacement of each element are obtained via the Standard & Explicit module of ABAQUS. Then, the stress acting on the RVE boundary is obtained by dividing the sum of the associated directional nodal forces generated at the boundary nodes by the area of the affected boundary. This stress value is subsequently used to estimate the homogenized Young's modulus of the RVE by dividing it by the applied strain. For example, the equivalent Young's modulus of the RVE along the x-axis is calculated by [40]:

$$E_1 = \frac{\sum_i^n f_{11}^{(i)}}{O_y\cdot O_z\cdot E_{11}} \tag{77}$$

where n represents the total number of nodes on the boundary perpendicular to the x-axis, and f_{11} represents the x-directional nodal force of boundary nodes. At the same time, the transverse strains caused by the axial force are obtained by using the nodal displacement data, from which the equivalent Poisson ratios of the RVE are obtained by dividing the transverse strains by the applied axial strain. Similarly, the equivalent shear moduli are estimated by dividing the shear stress values by the shear strains applied in the two corresponding directions. Once the equivalent moduli and equivalent Poisson ratios are obtained, the equivalent elastic constants of the RVE can be converted from the following relationship:

$$\boldsymbol{C} = \begin{bmatrix} C_{11} & C_{12} & C_{13} & 0 & 0 & 0 \\ & C_{22} & C_{23} & 0 & 0 & 0 \\ & & C_{33} & 0 & 0 & 0 \\ & & & C_{44} & 0 & 0 \\ & & & & C_{55} & 0 \\ & & & & & C_{66} \end{bmatrix} = \boldsymbol{S}^{-1} \tag{78}$$

where $\boldsymbol{S}$ denotes the compliance matrix of the orthotropic material:

$$\boldsymbol{S} = \begin{bmatrix} \frac{1}{E_1} & -\frac{v_{12}}{E_2} & -\frac{v_{13}}{E_3} & 0 & 0 & 0 \\ -\frac{v_{21}}{E_1} & \frac{1}{E_2} & -\frac{v_{23}}{E_3} & 0 & 0 & 0 \\ -\frac{v_{31}}{E_1} & -\frac{v_{32}}{E_2} & \frac{1}{E_3} & 0 & 0 & 0 \\ 0 & 0 & 0 & \frac{1}{G_{23}} & 0 & 0 \\ 0 & 0 & 0 & 0 & \frac{1}{G_{13}} & 0 \\ 0 & 0 & 0 & 0 & 0 & \frac{1}{G_{12}} \end{bmatrix} \tag{79}$$

Fig. 10 presents stress distribution maps and deformation modes of the RVE corresponding to the six macroscopic strains that are applied individually. Table 2 compares the equivalent properties deduced theoretically and those obtained via FE simulations. Except for C_{13} and C_{23}, the theoretical results are in good agreement with the simulation results. Theoretically, given that the volume fraction of the honeycomb $\lambda_H \ll 1$, Shi et al. [39] assumed the transverse Poisson ratios $v_{31} = v_{32} = 0$ such that the honeycomb equivalent properties C_{13}^H and C_{23}^H are equal to zero, as shown in Eq. (43). However, this assumption is not considered in the present FE analysis, thus leading to the discrepancy between the theoretical and FE results in Table 2. Nonetheless, it is worth noting that, for C_{13} and C_{23}, although the assumption of zero Poisson ratios causes certain discrepancies between theoretical and the FE results, its influence on the natural frequency of the hybrid-cored sandwich plate is negligible (more details presented later in Section 5.2).

Next, to ensure the convergence of the proposed method, the effect of RVE size on the equivalent properties of the hybrid core is investigated. As shown in Fig. 11(a), four RVEs containing 1×1, 2×2, 3×3, and 4×4 periodic unit cells respectively are established to represent the change of RVE size. In the theoretical method, the same setting of RVE size is adopted. Fig. 11(b) to (d) plot both the theoretically predicted (red solid lines) and numerically simulated (black dotted lines) equivalent properties as functions of RVE size. It can be seen that the proposed theoretical method and the FE simulation both exhibit excellent convergence.

5. Results and discussion

Hitherto, a 3D model of free vibration for novel ultralight sandwich plates with homogenized honeycomb-corrugated hybrid cores has been established. This section attempts to (1) determine the stiffnesses of the introduced springs for classical boundary conditions; (2) verify the accuracy and convergence of the proposed theoretical model; (3) analyze the influence of key geometric parameters on the natural frequency of the hybrid-cored sandwich plate; (4) compare its frequency response with those of honeycomb sandwich plate and an empty (unfilled) corrugated sandwich plate having equal mass; (5) study the effect of hybrid design on structure weight. To this end, detailed geometric parameters of an all-metallic hybrid-cored sandwich plate are given in Table 3. The material make of the whole sandwich (faces, corrugated plate, and honeycomb) is Al, which has the following material properties: Young's modulus $E_0 = 70$ GPa, Poisson ratio $v_0 = 0.3$, and mass density $\rho_0 = 2700$ kg/m^3.

5.1. Determination of spring stiffness

As shown schematically in Fig. 8(a), upon introducing uniformly distributed elastic springs at the 4 edges of the sandwich plate, its boundary conditions can be easily altered by assigning specific values to the stiffnesses of these springs. Theoretically, the classical boundary conditions such as simply supported and fully clamped can be realized

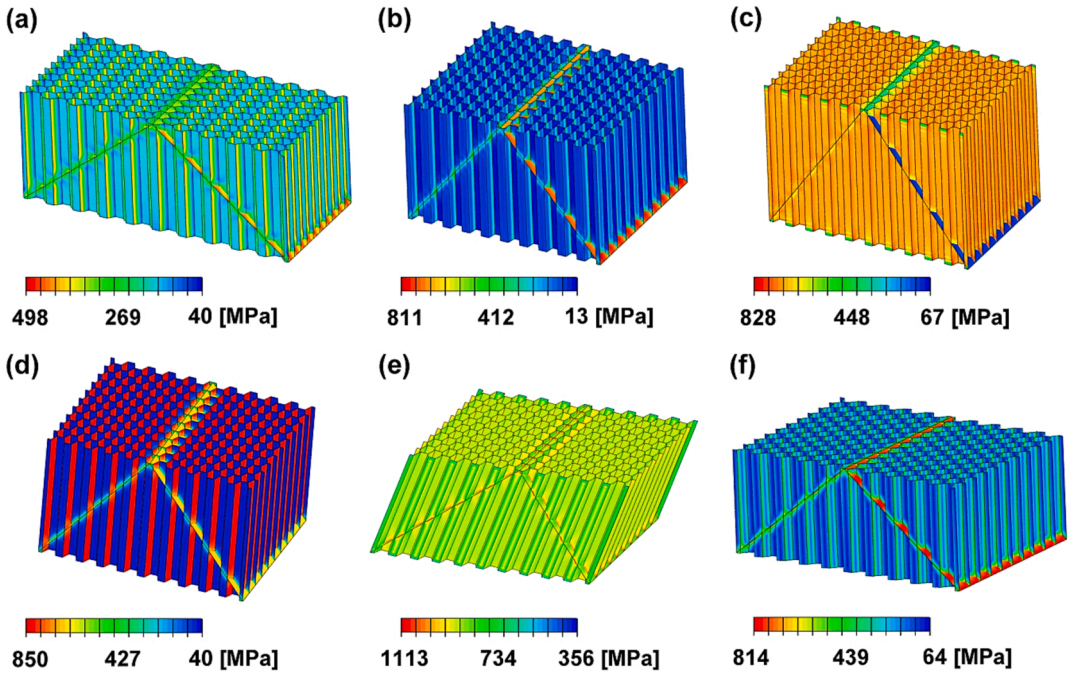

Fig. 10. Stress distribution map and deformation mode of the RVE corresponding to macroscopic strain: (a) E_{11}; (b) E_{22}; (c) E_{33}; (d) E_{23}; (e) E_{13}; (f) E_{12}.

Table 2
Comparison between equivalent properties deduced by theoretical method and FE simulation.

Method	Equivalent elastic properties [GPa]								
	C_{11}	C_{12}	C_{13}	C_{22}	C_{23}	C_{33}	C_{44}	C_{55}	C_{66}
Present	3.244	2.842	0.092	5.850	0.060	11.237	2.098	3.071	0.723
FE	3.414	2.897	2.330	5.840	1.981	11.466	2.042	3.000	0.719

only when the stiffnesses of the corresponding springs are infinite. As it is not convenient to numerically process infinitely large values, setting reasonable stiffness values to the springs is necessary to ensure the accuracy of calculation results. Fig. 9 plots the non-dimensional fundamental frequency of honeycomb-corrugated sandwich plate as a function of spring stiffness for selected boundary conditions. The non-dimensional frequency parameter λ is defined as:

$$\lambda = \omega ab \Big/ \pi^2 \sqrt{(\rho_0 h)/D_0};\ D_0 = E_0 h^3 \Big/ \left[12\left(1-\nu_0^2\right)\right] \tag{80}$$

Note that, in subsequent numerical examples, all frequency parameters are denoted in the non-dimensional form of (80). It can be seen from Fig. 12 that, regardless of the type of boundary conditions considered, the fundamental frequency converges gradually when the spring stiffness is greater than 1e16. Therefore, conservatively, 1e17 is taken in the current study as the spring stiffness to represent classical boundary conditions. A similar conclusion was reached in our previous study [41]. Spring stiffness values thus identified for three classical boundary conditions, i.e., free (referred to as F), simply supported (referred to as S), and clamped (referred to as C), are summarized in Table 4.

5.2. Convergence and accuracy

To solve the problem of free vibration under arbitrary boundary conditions, the displacements of the honeycomb-corrugated sandwich plate are expressed as 3D Fourier series. The dimensionality of the eigenvalue equation (73) is directly dependent upon the number of series expansion terms: when the number tends to infinity, the eigenvalues gradually converge to the exact solution. However, too many expansion terms would greatly reduce the computational efficiency, so it is necessary to carry out a convergence study to determine a suitable truncated number of the Fourier series. Table 5 shows how the first six natural frequencies of a CFSF hybrid sandwich plate vary with the truncated number. The theoretical calculation results are compared with those obtained by performing FE simulations via the commercially available FE code ABAQUS. Further, based on the first-order shear deformation theory (FSDT) [42], the frequency response of the hybrid sandwich plate calculated using a three-layer laminate model is also presented in Table 5 to demonstrate the accuracy of the method proposed in the present study.

Since the thickness of the face sheets, corrugated plates, and honeycomb cell walls are much smaller than the macro-dimensions of the honeycomb-corrugated sandwich plate, the FE model is constructed using shell elements (linear quadrilateral element S4R in ABAQUS nomenclature). To ensure the accuracy of the model, there should be at least 4 elements in the honeycomb wall length, and the FE meshing is shown in Fig. 13(a). In particular, geometrical parameters of the model for theoretical calculation and FE analysis are reset, as summarized in Table 6, because an excessively large geometric model significantly increases the number of FE grids and makes the simulation calculation difficult to complete.

The results of Table 5 demonstrate that, when the truncated number of the 3D Fourier series exceeds $18 \times 18 \times 9$, the theoretical results converge and are consistent with the FE simulation results. For other boundary conditions, the convergence and accuracy of the theoretical model are also considered, as detailed in Appendix A. Therefore, $M \times N \times L = 18 \times 18 \times 9$ is selected as the default truncated number in subsequent analysis. Fig. 13(b) and (c) display the first four transverse vibration modes of a CFSF hybrid-cored sandwich plate obtained using the proposed theoretical model and FE simulation, respectively. The vibration modes obtained by the two approaches are completely consistent,

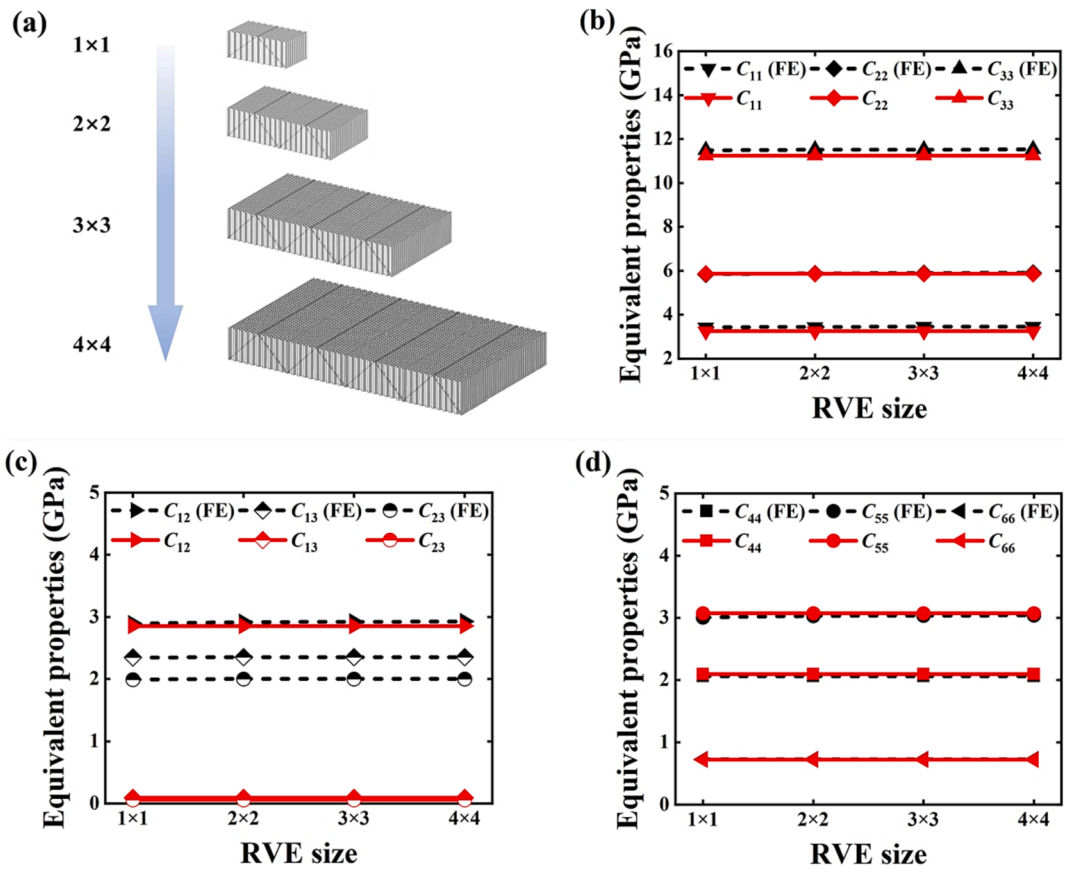

Fig. 11. (a) RVEs containing 1 × 1, 2 × 2, 3 × 3, and 4 × 4 periodic unit cells. Equivalent properties of hybrid core plotted as a function of RVE size: (b) C_{11}, C_{22}, C_{33}; (c) C_{12}, C_{13}, C_{23}; (d) C_{44}, C_{55}, C_{66}. Red solid line: theoretical method. Black dotted line: FE simulation. (For interpretation of the references to color in this figure legend, the reader is referred to the web version of this article.)

Table 3
Geometric parameters of honeycomb-corrugated sandwich plate.

t_H	l_H	Φ	t_C	θ	d	t_f	t_{core}	a	b
0.1 mm	1.5 mm	120°	1 mm	45°	0 mm	1 mm	15 mm	200 mm	200 mm

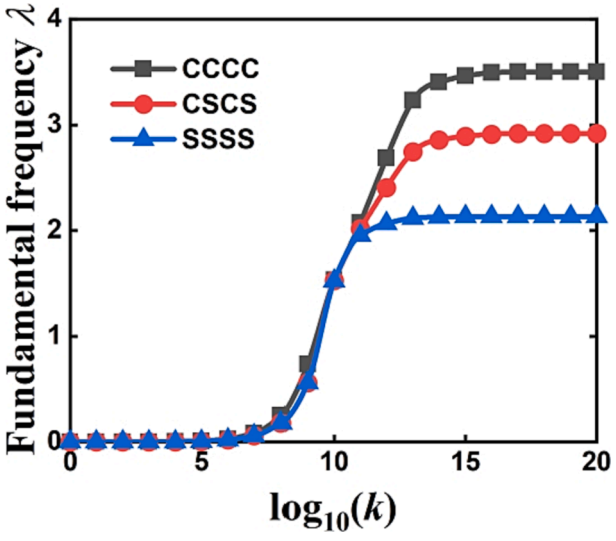

Fig. 12. Non-dimensional fundamental frequency of honeycomb-corrugated sandwich plates plotted as a function of spring stiffness for three different boundary conditions.

Table 4
Spring stiffness setup for classical boundary conditions.

Mark number	Edge	Boundary condition	Spring stiffness [N/m]		
			ku	*kv*	*kw*
(1)	$x = 0$	Free (F)	0	0	0
(1)	$x = 0$	Simply supported (S)	0	1e17	1e17
(1)	$x = 0$	Clamped (C)	1e17	1e17	1e17
(2)	$y = 0$	Free (F)	0	0	0
(2)	$y = 0$	Simply supported (S)	1e17	0	1e17
(2)	$y = 0$	Clamped (C)	1e17	1e17	1e17
(3)	$x = a$	Free (F)	0	0	0
(3)	$x = a$	Simply supported (S)	0	1e17	1e17
(3)	$x = a$	Clamped (C)	1e17	1e17	1e17
(4)	$y = b$	Free (F)	0	0	0
(4)	$y = b$	Simply supported (S)	1e17	0	1e17
(4)	$y = b$	Clamped (C)	1e17	1e17	1e17

thus verifying the accuracy of the theoretical model proposed in the present study. In contrast, the three-layer laminate model based on the FSDT leads to significant errors compared with the present method, thus indicating that the latter is more accurate for sandwich plates with relatively thick cores.

Next, to evaluate the accuracy of the corrected honeycomb

Table 5
Convergence and accuracy study of non-dimensional frequency parameter λ for a CFSF hybrid-cored sandwich plate.

$M \times N \times L$	Natural frequency					
	λ_1	λ_2	λ_3	λ_4	λ_5	λ_6
$4 \times 4 \times 2$	0.420	0.912	1.558	1.589	1.812	2.541
$8 \times 8 \times 4$	0.366	0.882	1.134	1.360	1.789	2.226
$12 \times 12 \times 6$	0.357	0.876	1.101	1.320	1.784	2.155
$16 \times 16 \times 8$	0.354	0.874	1.089	1.303	1.782	2.126
$17 \times 17 \times 9$	0.353	0.874	1.087	1.302	1.781	2.123
$18 \times 18 \times 9$	0.353	0.874	1.086	1.301	1.781	2.121
FE	0.353	0.874	1.081	1.288	1.782	2.099
FSDT	0.358	0.876	1.129	1.382	1.789	2.267

equivalent stiffness, the frequency response of the hybrid sandwich plate calculated based on the formulae of Ref. [20] is compared with the results obtained using the present method. Table 7 lists the first six order natural frequency responses of hybrid sandwich plates under different boundary conditions. The geometric parameters are the same as those in Table 6. Results show that using the incorrect honeycomb equivalent stiffness of Ref. [20] causes relatively large errors to natural frequencies; further, with the increasing order of natural frequency, the error gradually increases. In addition, the stronger the boundary constraint, the larger the error.

5.3. Influence of geometric parameters

Compared with material properties and boundary conditions, the geometric configuration of a honeycomb-corrugated sandwich plate is more complicated. It is therefore necessary to systematically study how geometric parameters affect the free vibration characteristics so that the role played by each geometric parameter can be clarified; the remaining parameters are consistent with Table 3.

Fig. 14(a) plots the fundamental frequency of the CCCC honeycomb-corrugated sandwich plate as a function of corrugated angle θ for selected ratios of corrugated thickness to face thickness, t_C/t_f. The corrugated angle is varied within a practically attainable range, from 30° to75°. The fundamental frequency first increases, reaching a peak, and then decreases as t_C/t_f is increased. As described in the governing equation of (73), the fundamental frequency of the sandwich plate increases with increasing bending stiffness and decreases with increasing mass density. When the corrugated angle θ is increased, both the bending stiffness and mass density of the sandwich plate increase. Fig. 14(b) plots the ratio of hybrid core relative density to the normalized base material density, ρ_{core}/ρ_0, as a function of corrugated angle θ for selected values of t_C/t_f. When the corrugated angle is small, the relative density changes little, and the fundamental frequency increases with increasing bending stiffness. When the corrugated angle becomes sufficiently large, the relative density increases rapidly, and the fundamental frequency decreases as the relative density is increased. In addition, it can be seen from Fig. 14(a) that the greater the corrugated thickness, the smaller the fundamental frequency, implying that the influence of increased bending stiffness on fundamental frequency as a result of enlarged corrugated thickness is small; on the contrary, because the mass of the hybrid core is increased, the fundamental frequency is reduced. In short, a proper corrugated angle can maximize the fundamental frequency of the hybrid-cored sandwich plate, and the influence of corrugated thickness on fundamental frequency is dominated by mass.

Fig. 15(a) plots the fundamental frequency of the CCCC honeycomb-corrugated sandwich plate as a function of corrugated length l_C (normalized by corrugated thickness t_C) for selected ratios of corrugated

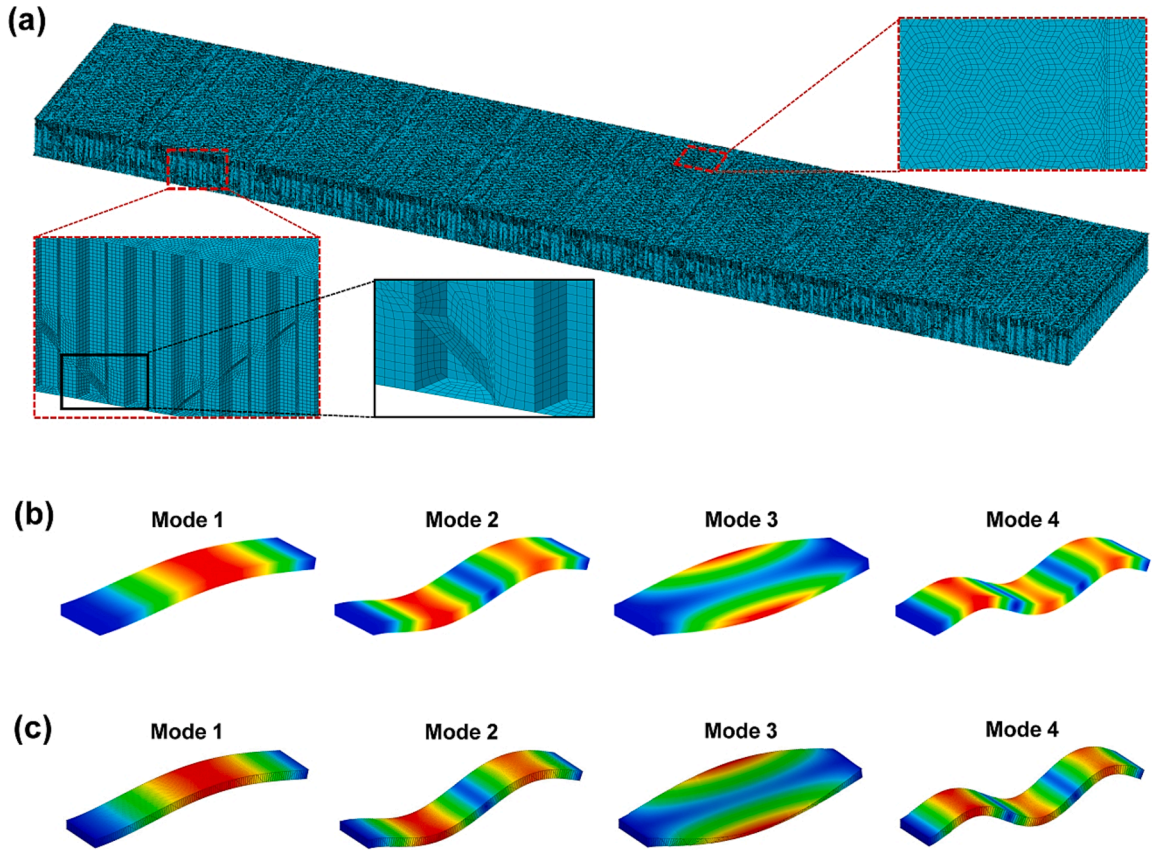

Fig. 13. (a) FE meshing of hybrid-cored sandwich plate and the first four transverse vibration modes of CFSF hybrid-cored sandwich plate obtained using (b) theoretical model and (c) 3D direct FE simulation.

Table 6
Geometric parameters of hybrid-cored sandwich plate for convergence and accuracy study.

t_H	l_H	Φ	t_C	θ	d	t_f	t_{core}	a	b
0.06 mm	1 mm	120°	0.6 mm	45°	3.6 mm	1.4 mm	11.4 mm	300 mm	58.89 mm

Table 7
Natural frequencies of hybrid sandwich plates under different boundary conditions: comparison between the method of Ref. [20] and the present method.

BCs	Method	Natural frequency					
		λ_1	λ_2	λ_3	λ_4	λ_5	λ_6
CCCC	present	5.949	6.192	6.641	7.314	8.186	9.239
CCCC	Ref. [20]	6.133	6.777	7.661	8.653	9.670	10.695
CFCF	present	0.505	1.182	1.305	1.333	2.375	2.678
CFCF	Ref. [20]	0.497	1.254	1.462	2.237	2.418	3.373
SFSF	present	0.228	0.598	0.879	1.271	1.868	2.093
SFSF	Ref. [20]	0.226	0.610	0.857	1.789	2.306	2.341

platform width d to corrugated thickness t_C. Since the volume fraction of corrugated core is a function of l_C and d, its mass and stiffness also vary with l_C and d. Therefore, in Fig. 15(b), the mass of the hybrid core is plotted as a function of l_C/t_C and d/t_C. In general, increasing the mass of a structure results in decreased natural frequency. The results of Fig. 15 reveal that the natural frequency and mass of the hybrid-cored sandwich plate increase monotonically with the increase of l_C, which means that increasing l_C also increases the bending stiffness of the plate such that the natural frequency is dominated by stiffness. This is because increasing l_C enlarges the thickness of the core, and the increase in bending stiffness of the sandwich is more significant than the increase in mass caused by core thickening. In addition, it is also found that the influence of corrugated platform d on core mass and natural frequency is small. It can be seen from the enlarged figure of Fig. 15(a) that the increase of d slightly reduces the natural frequency, but the mass remains almost unchanged, indicating that the increase of d slightly reduces the bending stiffness of the hybrid structure. This means that the effect of d on structural stiffness does not need to be concerned in the actual manufacturing process, as long as the selection of d ensures a good connection between the core and the face sheets.

Next, Fig. 16(a) and (b) plot separately the fundamental frequency as a function of honeycomb cell wall thickness t_H and length l_H, both normalized by corrugated thickness t_C, under different boundary conditions. The fundamental frequency is seen to decrease with increasing t_H and increase with increasing l_H. According to equation (1a), the volume fraction of the honeycomb is proportional to t_H and inversely proportional to l_H. This means that, when t_H is increased, the mass of the hybrid core is also increased, resulting in a decrease in fundamental frequency; when l_H is increased, the mass of the hybrid core is reduced, thus increasing fundamental frequency. Although changing the

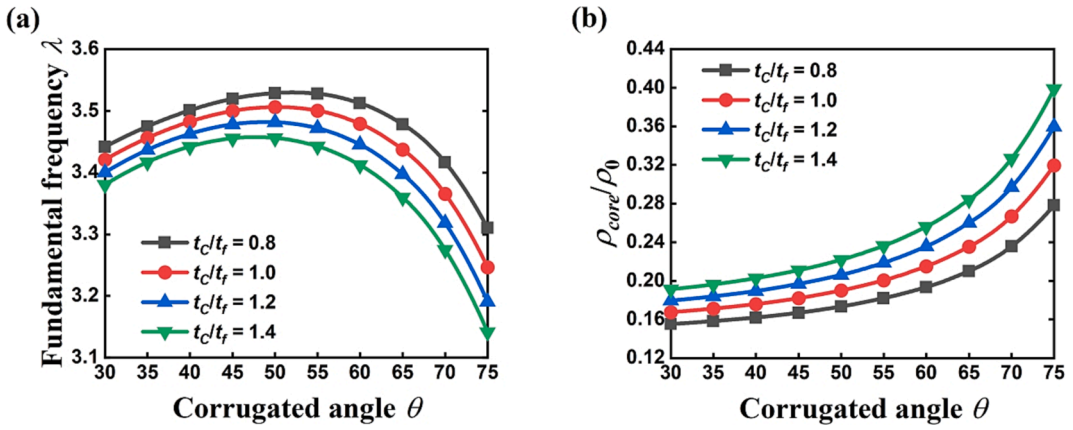

Fig. 14. (a) Dimensionless fundamental frequency and (b) normalized hybrid core relative density plotted as functions of corrugated angle θ for CCCC honeycomb-corrugated sandwich plates with different corrugated thicknesses.

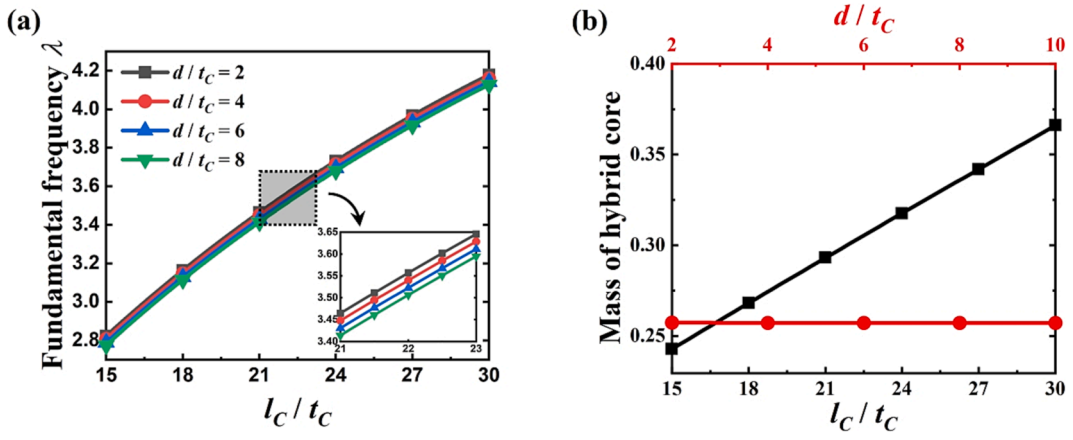

Fig. 15. (a) Fundamental frequency of a CCCC honeycomb-corrugated sandwich plate plotted as a function of normalized corrugated length l_C/t_C for selected values of corrugated platform width d/t_C. (b) Mass of hybrid core plotted as a function of l_C/t_C and d/t_C.

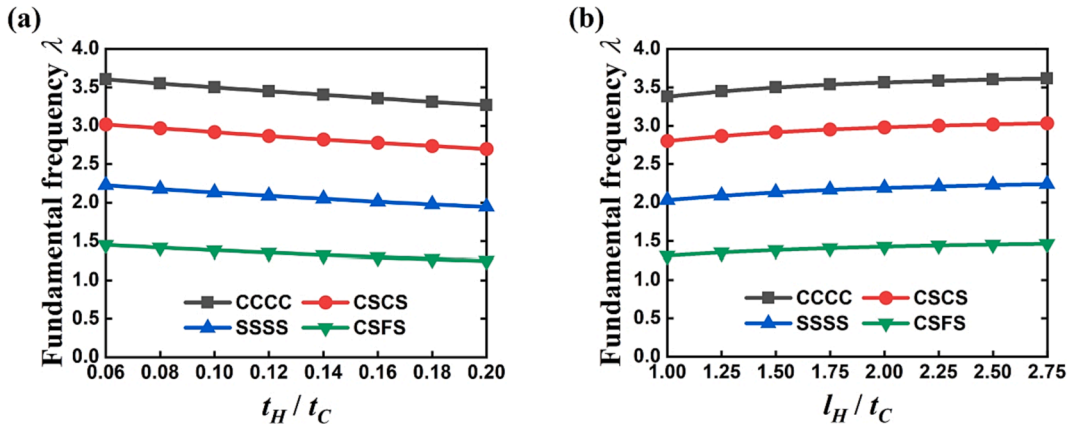

Fig. 16. Fundamental frequency of honeycomb-corrugated sandwich plate plotted as a function of (a) honeycomb wall thickness t_H and (b) honeycomb wall length l_H, both normalized by corrugated thickness, t_C, under different boundary conditions.

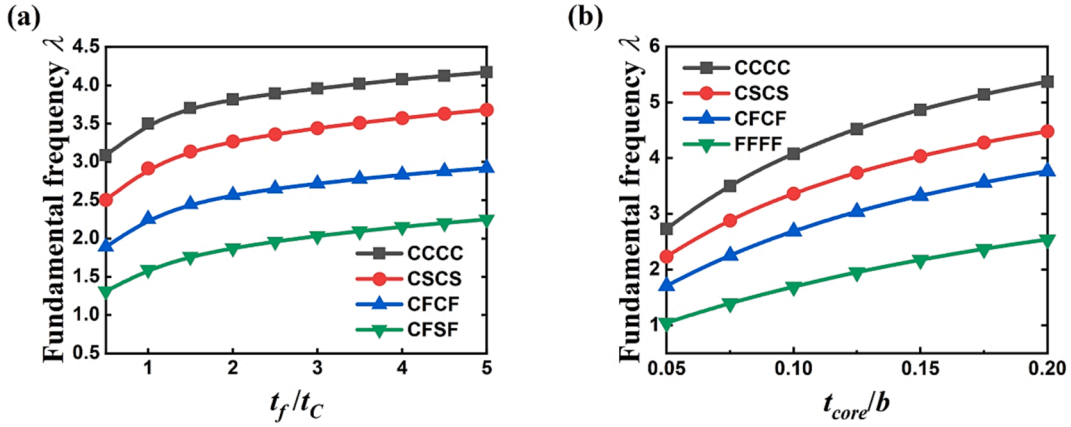

Fig. 17. Fundamental frequency of honeycomb-corrugated sandwich plate changes with the thickness of (a) face sheets and (b) hybrid core under different boundary conditions.

geometric parameters of the honeycomb will also change the bending stiffness of the hybrid core, the latter has much less influence on natural frequency than the mass, for the bending stress of the sandwich plate is mainly borne by its face sheets.

Finally, the fundamental frequency of the honeycomb-corrugated sandwich plate is plotted in Fig. 17(a) as a function of face sheet thickness t_f (normalized by corrugated thickness t_C) under different boundary conditions. It can be found that with the increase of t_f, the fundamental frequency increases monotonically. Fig. 17(b) plots the fundamental frequency as a function of the normalized thickness of the hybrid core under different boundary conditions. Same as Fig. 17(a), the fundamental frequency increases monotonically with increasing core thickness. This is because the increase of either face sheet thickness or core thickness will significantly increase the bending stiffness of the sandwich. Therefore, face sheet and core thicknesses play a more significant role in the free vibration of a hybrid-cored sandwich plate.

Table 8
Geometric parameters of sandwich plates with three different cores.*

Core	Geometric parameters [mm]								
	t_H	l_H	Φ	t_C	d	t_f	t_{core}	a	b
Hybrid	0.1	1.5	120°	1	0	1	15	245	163
Honeycomb		1.5	120°	–	–	1	15	245	163
Corrugated	–	–	–		0	1	15	245	163

* ' – ' denotes parameters not included in core geometry.

5.4. Comparison between hybrid-cored sandwich plate with competing sandwich plates

Through the above analysis of geometrical parameters, it is established that the influence of corrugated thickness, honeycomb cell wall thickness, and honeycomb cell wall length on the natural frequency of honeycomb-corrugated sandwich plate is dominated by mass. When changes in geometrical parameters cause the mass of the hybrid core to increase, the natural frequency decreases. To further explore the superiority of hybrid-core design, as the corrugated angle is systematically varied, the first three natural frequencies obtained using the proposed theoretical model for the honeycomb-corrugated sandwich plate are compared with those of both honeycomb and empty corrugated sandwich plates having equal mass. Relevant geometric parameters of the three different sandwich plates are presented in Table 8, and the data not shown are obtained by converting the mass of the hybrid-cored sandwich plate.

It should be noted that, based on the present theoretical model, while the natural frequency of a honeycomb sandwich plate can be obtained by setting the corrugated thickness to zero, the natural frequency of an empty corrugated sandwich plate cannot be obtained by setting the honeycomb wall thickness to zero. Because the unfilled interstices of the corrugated core lack effective support for both face sheets, the empty

Table 9
Comparison of theoretical natural frequencies of a honeycomb sandwich beam with existing experimental and numerical results [43].

Source	Natural frequencies [Hz]		
	Mode 1	Mode 2	Mode 3
Exp. [43]	1107	2900	5043
FE [43]	1235.2	3041.5	5336.2
Present	1231.4	3067.8	5377.1

Table 10
Comparison of numerical natural frequencies of a corrugated sandwich plate with existing experimental and numerical results [7].

Source	Natural frequencies [Hz]		
	Mode 1	Mode 2	Mode 3
Exp. [7]	615.2	693.4	1015.6
FE [7]	616.75	728.13	1057.6
Present	616.45	742.75	1106.2

corrugated sandwich plate is prone to local vibration modes, which cannot be considered by the method of homogenization. Therefore, for the purpose of comparison, the natural frequency of empty corrugated sandwich plate is obtained via 3D direct FE simulations.

To verify the accuracy of the proposed scheme, the theoretical results of a honeycomb sandwich beam are compared with existing experimental and simulation results [43] (Table 9), while the simulation results of a corrugated sandwich plate are compared with existing experimental and simulation results [7] (Table 10). Geometric parameters of the honeycomb sandwich and the corrugated sandwich are consistent with Ref. [43] and Ref. [7], respectively. The results of Tables 9 and 10 demonstrate that the present results agree well with those in the open literature, thus confirming the accuracy of the proposed scheme.

In Fig. 18, the first three natural frequencies of the CCCC honeycomb-corrugated sandwich plate, honeycomb sandwich plate, and empty corrugated sandwich plate having equal mass are plotted as a function of corrugated angle. Within the considered corrugated angle range (40°∼75°), the natural frequencies of the honeycomb-corrugated sandwich plate are always greater than those of either honeycomb or empty corrugated sandwich plate, because honeycomb filling suppresses local vibration of the face sheets and corrugated members, and the mutual constraint between honeycomb and corrugation enhances the flexural rigidity of the hybrid core. This demonstrates again that the proposed honeycomb-corrugated hybrid sandwich construction not only exhibits excellent specific stiffness/strength, energy absorption, and sound attenuation as previously reported [17–19] but also is endowed with superior vibration characteristics. When the corrugated angle is reduced, the natural frequency of empty corrugated sandwich decreases significantly due to the local vibration modes of its face sheets; Fig. 19. When the corrugated angle becomes sufficiently large, the first-order natural frequency of the empty corrugated sandwich is greater than the honeycomb sandwich but smaller than the honeycomb-corrugated sandwich. This is because although the larger corrugated angle increases the bending rigidity of the corrugated core, local vibration modes of the face sheets and the lack of honeycomb-corrugated coupling caused the fundamental frequency to drop below that of a hybrid-cored sandwich. For a honeycomb sandwich with the same mass, increasing the mass of the honeycomb core reduces its natural frequency. Different from the first-order natural frequency of Fig. 18(a), in Fig. 18(b) and (c), the second- and third-order natural frequencies of honeycomb

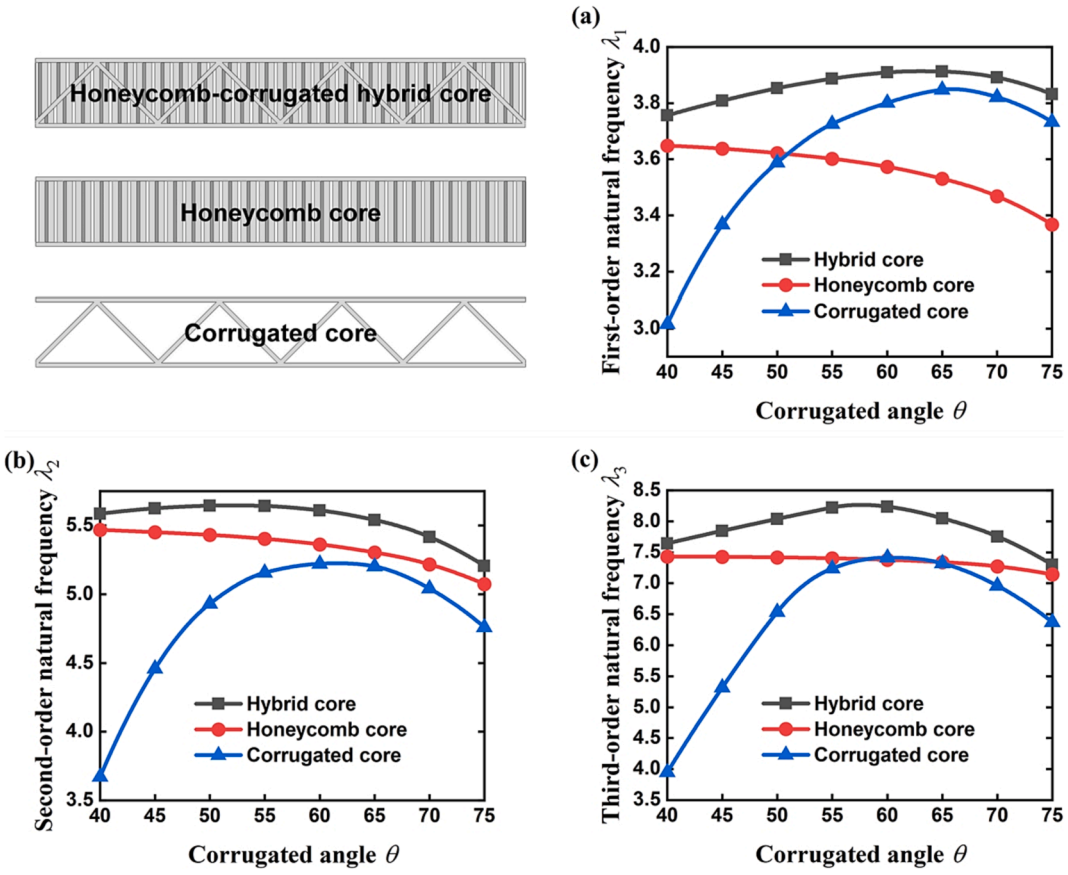

Fig. 18. First three natural frequencies of CCCC honeycomb-corrugated sandwich plate, honeycomb sandwich plate, and an empty corrugated sandwich plate having equal mass plotted as functions of corrugated angle: (a) first-order; (b) second-order; (c) third-order.

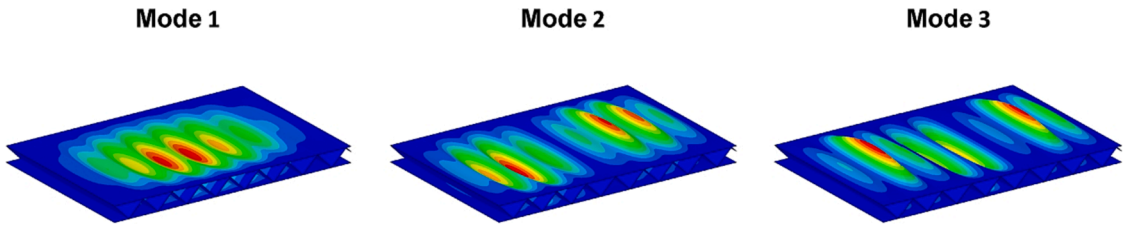

Fig. 19. First three vibration modes of CCCC empty corrugated sandwich plate with a corrugated angle of 45°.

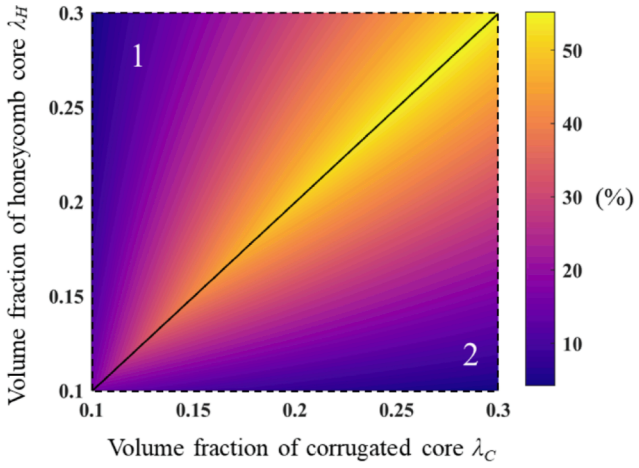

Fig. 20. Dependence of weight increase of hybrid structure on volume fraction of honeycomb core and volume fraction of corrugated core.

sandwiches are consistently larger than those of empty corrugated sandwiches. This may be because the large corrugated angle suppresses low-order local vibration modes of empty corrugated sandwich, but cannot suppress the higher-order ones.

Finally, the effect of hybrid design on structure weight is studied. To this end, sandwich structures with a honeycomb core, a corrugated core, and a honeycomb-corrugated hybrid core are selected as examples. The length, width, height, face sheet thickness, and material properties of the three sandwich structures are set to be the same, whereas the volume fraction of honeycomb core and that of corrugated core are varied. As shown in Fig. 20, the vertical axis represents the volume fraction of honeycomb core (λ_H) and the horizontal axis represents the volume fraction of corrugated core (λ_C), both varying in the range of $0.1 \sim 0.3$. The color of point (λ_C, λ_H) in region 1 indicates the weight increase (%) of the hybrid sandwich relative to the corrugated sandwich. Similarly, the color of any point in area 2 indicates the weight increase (%) of the hybrid sandwich relative to the honeycomb sandwich. The results of Fig. 20 demonstrate that the larger the volume fraction difference between honeycomb and corrugated cores, the smaller the mass increase of the resulting hybrid structure. This is one of the reasons why we use Al honeycomb instead of Al foam to fill the interstices of corrugated core. It must however be pointed out that, with minimal increase in mass, the proposed hybrid design can not only significantly increase the stiffness, strength (peak load), energy absorption, and sound absorption of the sandwich construction, but also lead to superior free vibration performance.

6. Concluding remarks

Based on the theory of 3D elasticity, a theoretical model has been developed to predict the free vibration performance of a novel multi-functional honeycomb-corrugated sandwich rectangular plate, with arbitrary boundary conditions considered using sets of elastic springs. The method of homogenization is utilized to establish the equivalent elastic constants of the hybrid core, with the correct equivalent constitutive equations of honeycomb employed and the coupling effect between inserted honeycomb blocks and corrugated members duly accounted for based on micromechanics analysis of its RVE (representative volume element). Convergence and accuracy of the proposed model are validated against finite element (FE) simulations for different boundary conditions, with excellent agreement achieved.

The validated theoretical model is adopted to quantify the effects of corrugated angle, corrugated thickness, corrugated length, width of corrugated platform, honeycomb wall thickness, honeycomb wall length, core thickness, and face sheet thickness on free vibration characteristics of the hybrid-cored sandwich. It is demonstrated that filling honeycomb blocks to the interstices of corrugations not only can lead to significantly enhanced stiffness, strength, impact energy absorption, and sound absorption but also superior free vibration performance, with minimal increase in structural mass. The natural frequencies of honeycomb-corrugated sandwich construction are consistently higher than its counterparts - honeycomb sandwich and empty corrugated sandwich of equal mass. This is mainly attributed to mechanisms: (1) honeycomb filling suppresses local vibration of the face sheets and corrugated members, and (2) mutual constraint of honeycomb and corrugation enhance the flexural rigidity of hybrid core. The proposed theoretical model can be easily extended to other cases, such as sound radiation and sound insulation analysis of honeycomb-corrugated sandwich plates.

CRediT authorship contribution statement

Rui Kang: Investigation, Writing – original draft, Software, Data curation. **Cheng Shen:** Resources, Validation, Writing – review & editing. **Tian Jian Lu:** Writing – review & editing, Resources, Supervision.

Declaration of Competing Interest

The authors declare that they have no known competing financial interests or personal relationships that could have appeared to influence the work reported in this paper.

Data availability

Data will be made available on request.

Acknowledgments

This research was supported by the National Natural Science Foundation of China (11502110, 11972185, 12032010); the Natural Science Foundation of Jiangsu Province (BK20150737); the Open Fund of the State Key Laboratory for Strength and Vibration of Mechanical Structures (SV2018-KF-01); and the Open Fund of the State Key Laboratory of Mechanics and Control of Mechanical Structures (MCMS-E0219K02, MCMS-I-0219K01, MCMS-I-0222K01).

Appendix A. Supplementary material

Supplementary data to this article can be found online at https://doi.org/10.1016/j.compstruct.2022.115990.

References

[1] Knox EM, Cowling MJ, Winkle IE. Adhesively bonded steel corrugated core sandwich construction for marine applications. Mar Struct 1998;11(4-5):185–204.
[2] Ng CF, Zheng H. Sound transmission through double-leaf corrugated panel constructions. Appl Acoust 1998;53(1-3):15–34.
[3] Liang C-C, Yang M-F, Wu P-W. Optimum design of metallic corrugated core sandwich panels subjected to blast loads. Ocean Eng 2001;28(7):825–61.
[4] Martinez OA, Sankar BV, Haftka RT, Bapanapalli SK, Blosser ML. Micromechanical analysis of composite corrugated-core sandwich panels for integral thermal protection systems. AIAA J 2007;45(9):2323–36.
[5] Dayyani I, Shaw AD, Saavedra Flores EI, Friswell MI. The mechanics of composite corrugated structures: a review with applications in morphing aircraft. Compos Struct 2015;133:358–80.
[6] Meng H, Galland MA, Ichchou M, Bareille O, Xin FX, Lu TJ. Small perforations in corrugated sandwich panel significantly enhance low frequency sound absorption and transmission loss. Compos Struct 2017;182:1–11.
[7] Wang X, Li X, Yu R-P, Ren J-W, Zhang Q-C, Zhao Z-Y, et al. Enhanced vibration and damping characteristics of novel corrugated sandwich panels with polyurea-metal laminate face sheets. Compos Struct 2020;251:112591.
[8] Ma Q, Rejab MRM, Siregar JP, Guan Z. A review of the recent trends on core structures and impact response of sandwich panels. J Compos Mater 2021;55(18):2513–55.
[9] Vaziri A, Xue Z, Hutchinson JW. Metal sandwich plates with polymer foam-filled cores. J Mech Mater Struct 2006;1:97–127.
[10] Yan LL, Yu B, Han B, Chen CQ, Zhang QC, Lu TJ. Compressive strength and energy absorption of sandwich panels with aluminum foam-filled corrugated cores. Compos Sci Technol 2013;86:142–8.
[11] Han B, Yan LL, Yu B, Zhang QC, Chen CQ, Lu TJ. Collapse mechanisms of metallic sandwich structures with aluminum foam-filled corrugated cores. J Mech Mater Struct 2014;9:397–425.
[12] Yan LL, Han B, Yu B, Chen CQ, Zhang QC, Lu TJ. Three-point bending of sandwich beams with aluminum foam-filled corrugated cores. Mater Des 2014;60:510–9.
[13] Han B, Qin K-K, Yu B, Zhang Q-C, Chen C-Q, Lu TJ. Design optimization of foam-reinforced corrugated sandwich beams. Compos Struct 2015;130:51–62.
[14] Han B, Yu B, Xu Y, Chen C-Q, Zhang Q-C, Lu TJ. Foam filling radically enhances transverse shear response of corrugated sandwich plates. Mater Des 2015;77:132–41.
[15] Yu B, Han B, Ni CY, Zhang QC, Chen CQ, Lu TJ. Dynamic crushing of all-metallic corrugated panels filled with close-celled aluminum foams. J Appl Mech-Trans ASME 2015;82:011006.
[16] Yan LL, Yu B, Han B, Zhang QC, Lu TJ, Lu BH. Effects of aluminum foam filling on the low-velocity impact response of sandwich panels with corrugated cores. J Sandwich Struct Mater 2020;22(4):929–47.
[17] Han B, Qin K, Yu B, Wang B, Zhang Q, Lu TJ. Honeycomb-corrugation hybrid as a novel sandwich core for significantly enhanced compressive performance. Mater Des 2016;93:271–82.
[18] Han B, Wang W, Zhang Z, Zhang Q, Jin F, Lu T. Performance enhancement of sandwich panels with honeycomb–corrugation hybrid core. Theor Appl Mech Lett 2016;6(1):54–9.
[19] Tang Y, Li F, Xin F, Lu TJ. Heterogeneously perforated honeycomb-corrugation hybrid sandwich panel as sound absorber. Mater Des 2017;134:502–12.
[20] Zhang Z-J, Han B, Zhang Q-C, Jin F. Free vibration analysis of sandwich beams with honeycomb-corrugation hybrid cores. Compos Struct 2017;171:335–44.
[21] Carrera E, Brischetto S. A survey with numerical assessment of classical and refined theories for the analysis of sandwich plates. Appl Mech Rev 2009;62:010803.
[22] Kreja I. A literature review on computational models for laminated composite and sandwich panels. Open Eng 2011;1:59–80.
[23] Sayyad AS, Ghugal YM. On the free vibration analysis of laminated composite and sandwich plates: a review of recent literature with some numerical results. Compos Struct 2015;129:177–201.
[24] Vescovini R, D'Ottavio M, Dozio L, Polit O. Buckling and wrinkling of anisotropic sandwich plates. Int J Eng Sci 2018;130:136–56.
[25] Huang Q, Choe J, Yang J, Hui Y, Xu R, Hu H. An efficient approach for post-buckling analysis of sandwich structures with elastic-plastic material behavior. Int J Eng Sci 2019;142:20–35.
[26] Ginot M, D'Ottavio M, Polit O, Bouvet C, Castanié B. Benchmark of wrinkling formulae and methods for pre-sizing of aircraft lightweight sandwich structures. Compos Struct 2021;273:114387.
[27] Huang Q, Choe J, Yang J, Xu R, Hui Y, Hu H. The effects of kinematics on post-buckling analysis of sandwich structures. Thin-Walled Struct 2019;143:106204.
[28] Jin G, Su Z, Shi S, Ye T, Gao S. Three-dimensional exact solution for the free vibration of arbitrarily thick functionally graded rectangular plates with general boundary conditions. Compos Struct 2014;108:565–77.
[29] Zamani MH, Heidari-Rarani M, Torabi K. A novel graded auxetic honeycomb core model for sandwich structures with increasing natural frequencies. J Sandwich Struct Mater 2022;24(2):1313–39.
[30] Han B, Qin K-K, Zhang Q-C, Zhang Q, Lu TJ, Lu B-H. Free vibration and buckling of foam-filled composite corrugated sandwich plates under thermal loading. Compos Struct 2017;172:173–89.
[31] Bitzer T, editor. Honeycomb Technology. London: Chapman & Hall; 1997.
[32] Wang X, Yu R-P, Zhang Q-C, Li L, Li X, Zhao Z-Y, et al. Dynamic response of clamped sandwich beams with fluid-fillied corrugated cores. Int J Impact Eng 2020;139:103533.
[33] Yu R-P, Wang X, Zhang Q-C, Li L, He S-Y, Han B, et al. Effects of sand filling on the dynamic response of corrugated core sandwich beams under foam projectile impact. Compos B Eng 2020;197:108135.
[34] Wadley HNG. Multifunctional periodic cellular metals. Philos Trans A Math Phys Eng Sci 2006;364(1838):31–68.
[35] Hill R. Elastic properties of reinforced solids: Some theoretical principles. J Mech Phys Solids 1963;11(5):357–72.
[36] Liu T, Deng ZC, Lu TJ. Structural modeling of sandwich structures with lightweight cellular cores. Acta Mech Sin 2007;23(5):545–59.
[37] Lu T, Liu T, Deng Z. Thermoelastic properties of sandwich materials with pin-reinforced foam cores. Sci China Ser E: Technol Sci 2008;51(12):2059–74.
[38] Hohe J, Becker W. Effective stress-strain relations for two-dimensional cellular sandwich cores: homogenization, material models, and properties. Appl Mech Rev 2002;55:61–87.
[39] Shi G, Tong P. The derivation of equivalent constitutive equations of honeycomb structures by a two scale method. Comput Mech 1995;15(5):395–407.
[40] Omairey SL, Dunning PD, Sriramula S. Development of an ABAQUS plugin tool for periodic RVE homogenisation. Eng Comput 2019;35(2):567–77.
[41] Kang R, Xin F, Shen C, Lu TJ. 3D free vibration analysis of functionally graded plates with arbitrary boundary conditions in thermal environment. Adv Eng Mater 2022;24(5):2100636.
[42] Reddy JN, Chao WC. A comparison of closed-form and finite-element solutions of thick laminated anisotropic rectangular plates. Nucl Eng Des 1981;64(2):153–67.
[43] Pourriahi V, Heidari-Rarani M, Torabpour Isfahani A. Influence of geometric parameters on free vibration behavior of an aluminum honeycomb core sandwich beam using experimentally validated finite element models. J Sandwich Struct Mater 2022;24(2):1449–69.

Further reading

[44] Mantari JL, Oktem AS, Guedes Soares C. A new higher order shear deformation theory for sandwich and composite laminated plates. Compos B Eng 2012;43(3):1489–99.